Depth Discrimination of Optical Inhomogeneities in a Liquid Phantom using a 2D Planar Scanning Diffuse Optical Imaging System

A thesis submitted by

Geethika Weliwitigoda

In partial fulfillment of the requirements

for the degree of

Master of Science

in

BIOENGINEERING

TUFTS UNIVERSITY

August 2012

ADVISER:

Sergio Fantini, Ph.D., Department of Biomedical Engineering, Tufts University

Committee Members:

Mark Cronin-Golomb, Ph.D., Department of Biomedical Engineering, Tufts University

Eric Miller, Ph.D., Department of Electrical Engineering & Computer Science, Tufts University

Abstract

Near infrared diffuse optical imaging has been a subject of much research for breast cancer screening purposes. In this study, we are testing the performance of a method to discriminate the depths of inhomogeneities in a liquid phantom using a 2D planar scanning frequency domain diffuse optical imaging system. A specific subject of interest is the calibration curves which are used to calibrate the off-axis shift between two detectors and a depth value. In particular, we are assessing how accurately the simulation software replicates the liquid phantom for different variations in optical properties, source-detector configuration, and geometry. We also describe the data processing that is necessary before the depth calculations can be executed and the noise characterization of the liquid phantom. It was found that for the calibration curves used for the experiments under calculated black rod inhomogeneities of shallower and middle depths ($\sim\pm$ 8 mm for normalized depth (z/D) < .6). In contrast, the accuracy was significantly higher for deeper depths ($\sim\pm$ 3 mm for z/D > .6) . Also, we found that the depth calculation is not affected by the angle of the rod structure in the x-y plane, nor the angle of the rod structure in depth direction. Lastly, we developed a calibration curve based on experimental data and compared it to that derived through simulation. It was found that the experimental calibration curve related off-axis shift to depth more accurately than the simulation-derived calibration curves.

Acknowledgments

I would like to thank my adviser, Professor Sergio Fantini, for his guidance, knowledge, and wisdom throughout these past two years. By working for his lab, I not only attained invaluable knowledge about diffuse optics, but I have also become a better engineer. He teaches in a way that encourages us to think outside the norms in order to find solutions to complex engineering problems.

I would like to thank Professor Angelo Sassaroli, for his precious guidance as well. These past two years he has graciously helped me in understanding the diffuse optics field, and has provided me with a theoretical mindset that has made me better prepared to solve a plethora of engineering problems. I also treasure the interesting conversations we had about life, culture, and the world.

I would like to thank Jana Kainerstorfer whose insight was especially helpful at the latter stages of my thesis. In particular, I have learned a lot from her about optical instrumentation and performing experiments in the most efficient and informative manner.

I would like to thank all my lab mates, especially Michele, Bertan, Pami, Fridrik, and Roni. Their advice and willingness to help are greatly appreciated and cherished. Additionally, I will miss our casual conversations about school, sports, and life.

Table of Contents

Chapter I Diffuse Optical Mammography Introduction and Background

1.1 Introduction

Breast cancer has been a persistent disease in the United States and around the world. 12% of women in the U.S. will develop breast cancer in the course of their lifetime [1]. In fact, 210,203 women in the U.S. were diagnosed with breast cancer in 2008 [2]. Globally, breast cancer accounts for 16% of cancers among women, thereby making it the most common type of cancer among women [3]. Such high incidence rates make breast cancer a subject of much research in terms of treatment, prevention, and detection.

Presently, the gold standard for breast cancer screening is X-ray mammography. Although X-ray mammography has been an established screening technique for decades, there are numerous efficacy and compliancy issues that call for improvement. For instance, X-ray mammography machines expose the patient to harmful ionizing radiation and the compression required to increase image contrast causes discomfort. Additionally, 11% of X-ray mammograms carried out in the U.S. resulted in false-positives [4]. Along with the emotional and physical toll on the patient, these false-positives cost around $100 million per year [5]. Thus, complimentary imaging modalities such as magnetic resonance imaging (MRI) have become a pronounced area of research in hopes of improving breast screening accuracy [6].

Recent advances in the field of diffuse optical imaging (DOI) have made it possible to acquire more physiological information than X-ray mammography in a manner that is comfortable and safe to the patient. Since DOI uses near-infrared light (NIR), the patient is not subjected to ionizing radiation and therefore does not pose a health risk. Furthermore, the harmlessness of NIR light and low operating cost make DOI systems ideal candidates for continuous monitoring applications.

The main premise behind optical mammography is to localize areas of the breast that exhibit specific biomarkers which signify diseased breast tissue. The two biomarkers that optical imaging is particularly sensitive to is angiogenesis and hypoxia. Breast tumors typically induce angiogenesis in order to alleviate the high nutrient and oxygen demand of the tumor cells. They also tend to be hypoxic as the cells consume oxygen significantly faster than healthy breast tissue. DOI imaging systems exploit the optical characteristics of NIR light in breast tissue to acquire spatial reconstructions of oxygenation that may highlight hypoxic and angiogenic areas within the sample.

However, one shortcoming of DOI is its inherent lack of spatial resolution due to the diffusive nature of NIR light in breast tissue. This is especially true for diffuse optical tomography (DOT), where the spatial resolution of the image reconstructions depend on the number of stationary source-detector pairs that surround the breast [7],[8],[9]. In order to account for spatial resolution, many studies have performed 2D planar scans where a collinear source and detector at opposite sides of a breast embedded between two plates scan in tandem the image space in the x-y plane [10],[11],[12]. The result of these scans are 2D projections of the image space. These scans achieve higher spatial resolution in the x-y plane (plane parallel to the plates) when compared with DOT image reconstructions primarily because of the fact that the spatial sampling rate is a controllable parameter. This is important in terms of breast cancer screening as higher resolution means that the radiologist will have more detailed structural and morphological information with which to make a diagnosis. Likewise, invasive breast cancer therapies require precise localization of tumor sites which can only be provided by high spatial resolution.

Since the images generated from the 2D planar scans are 2D projections of the image space in the x-y plane, they do not provide any information in the depth direction. One study that has developed a method in discriminating depth using an off-axis detector that is offset in the x-axis from the collinear detector by a specified amount [11]. The method measures the off-axis shift between the spatial location of an inhomogeneity in the images generated by both the on-axis and off-axis detectors. The depth is calculated by using a calibration curve which associates the off-axis shift to a specific depth. Although [11] discriminated the depths of carcinomas in human breast tissue, there has not been a study that fully characterizes the performance of the method to specific structural orientations and arrangements.

Thus, the purpose of this study is as follows:

- characterize the variance of the calibration curve that relates off-axis shift to depth when different medium geometries, source-detector configurations, and optical properties are used.

- develop a protocol for performing solid and liquid phantom 2D planar scans

- characterize the performance of the method for simple structural arrangements such as a single parallel rod

- characterize the performance of the method for more complex structural arrangements such as angled rods in all or a combination of axes and overlapping rods

Although breast tissue is composed of complex networks of arteries, veins, and lymphatic vessels, simple structural arrangements were used for this study to simplify the characterization of the depth discrimination method being tested. For instance, [11] and [12] both reported error between actual and calculated depths of the inhomogeneities they tested on. Therefore, the main motivation of this study is to identify trends in error that are associated with the spatial

arrangement of one rod inhomogeneity, as well as those due to optical property variation, and changes in the source-detector configuration. It is hoped that the information gained from this study will provide a foundation that can be used for further experimentation of more complex structural arrangements that can better emulate the environment in breast tissue.

1.2 Background

1.2.1 Light Tissue Interactions

There are two main types of light tissue interactions; absorption and scattering. Absorption occurs when the energy of an incident photon is transferred to an electron causing the electron to jump to a higher energy state. The proportion of incident light that is absorbed by a specific medium like breast tissue is portrayed by its absorption coefficient, μ_a, and is described as the inverse of the average path length before a photon is absorbed.

Absorption depends primarily on the wavelength of the NIR light, and the chromophores in the medium that interact with the incident photons. The expression below describes the absorption coefficient at a certain wavelength as the summation of absorption events from different chromophores.

$$\mu_a(\lambda) = \sum_{i=1}^{k} \varepsilon_i(\lambda) * C_i \tag{1.1}$$

where k indicates the number of chromophores, λ is the wavelength, ε is the extinction coefficient of the ith chromophore, and C_i is the concentration of the ith chromophore. Figure 1.1 shows the absorption spectra for the four main chromophores that comprise breast tissue; oxyhemoglobin (HbO_2), deoxyhemoglobin (Hb), lipid, and water.

Scattering occurs when a photon's trajectory changes due to a mismatch in the refractive index of the particles present in the medium. The scattering coefficient, μ_s, is defined as the inverse of the mean photon migration path between two consecutive scattering events. On the

other hand, the reduced scattering coefficient, μ_s', takes into account the photon paths are directional (towards the detector) close to the source fiber tip. Therefore, μ_s' is defined as the inverse of the mean photon migration path between two consecutive scattering events that have an isotropic possibility of post-scattering direction. The μ_s' of healthy breast tissue is generally between .2 to 1.5 m^{-1} [13].

The direction and amplitude of a scattering event is influenced by the morphology, size, and structure of scatterers that are within the medium. Eq. 1.2 demonstrates how μ_s' for a specific wavelength λ can be deduced with knowledge of μ_s' for a wavelength λ_o and the scattering power of the medium b.

$$\mu_s'(\lambda) = \mu_s'(\lambda_0) * \left[(\frac{\lambda}{\lambda_0})^{-b} \right] \tag{1.2}$$

Compared to absorption, scattering events are far more probable in breast tissue due to the abundance of these scatterers.
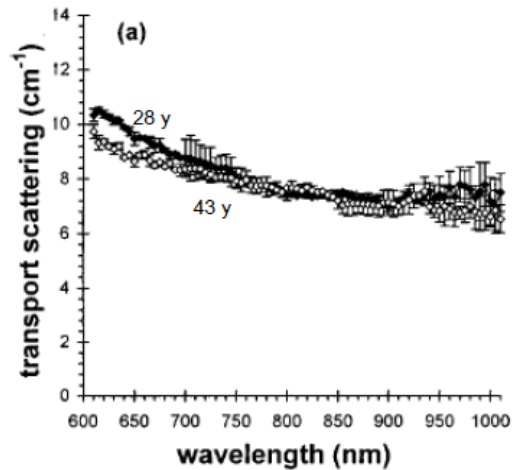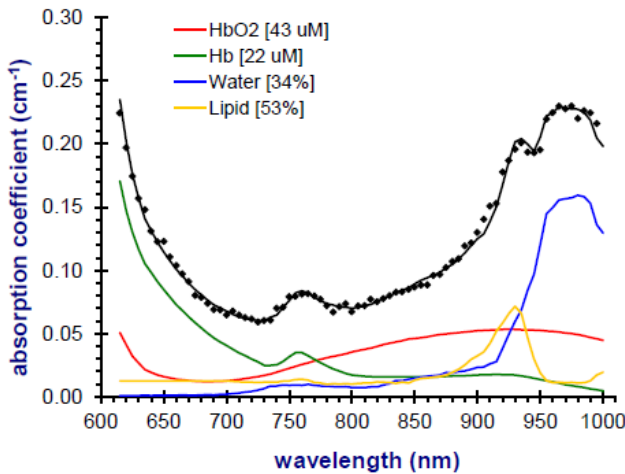
Figure 1.1. Absorption spectra for specified chromophore concentrations (left). Scattering spectra for the breasts of two women aged 28 years old (solid line) and 43 years old (circles) (right) [12].

1.2.2 Diffuse Optical Imaging

In general, Diffuse Optical Imaging (DOI) systems exploit this variance in absorption and scattering spectra to spatially reconstruct the concentrations of the aforementioned chromophores. As mentioned before, DOI systems utilize light in the near infrared region of the electromagnetic spectrum (600 - 1000 nm). NIR light is used in DOI mainly because of its high penetrability in tissue. Wavelengths that are shorter than this window experience excessive absorption by hemoglobin, whereas longer wavelengths experience excessive absorption by water [12].

DOI can utilize either a transmission or reflectance geometry for the source-detector configuration. A transmission source-detector configuration is when a coupled source and detector are at opposite sides of the biological tissue sample being imaged and the light transmits through the depth of the sample in order to be detected. In contrast, the source and detector are on the same side of a tissue sample in a reflectance geometry, and the detected photons are those that have been reflected back after tissue penetration. The choice of either one of these source-detector configurations depend mainly on the biological tissue being sampled as well as the purpose of the study. For instance, brain studies using DOI must use a reflectance geometry as the cross-distance of the human head is too far a distance for NIR photons to completely penetrate.

1.2.3 Diffuse Optical Mammography Systems

Presently, there are three types of optical mammography systems; continuous-wave (CW), time domain (TD), and frequency domain (FD) systems. Although the source of contrast described earlier is consistent among all three systems, what they differ in is the type of raw data acquired. Each has its advantages and disadvantages when it comes to processing, cost, and complexity and are compared in the following sections.

1.2.3.1 Continuous Wave

CW domain systems consists of a light source emitting a time-constant optical intensity and detector fibers coupled to either a photomultiplier tube or charge-coupled device. The source is generally that of a broadband light source in the NIR spectrum, thus providing rich spectroscopic imaging. CW domain systems also benefit from high signal-to-noise ratio (SNR). Compared to the other two mammography systems, CW domain systems are cheaper and simpler to implement.

Where CW domain systems primarily lack in is the amount of information that is acquired about the tissue in question. Since CW domain systems are geared to detect only the amplitude of the detected photon density waves, they are mainly sensitive to absorption changes. Therefore they cannot resolve between attenuation effects due to absorption and those due to scattering.

1.2.3.2 Time Domain

Time domain (TD) systems are more expensive to implement than CW systems, yet are able to distinguish between absorption and scattering. To achieve this discrimination, TD systems analyze the temporal point spread function (TPSF) of the photons that are detected using the time window analysis method [10].

The TPSF is the system's impulse response in the time domain. For instance, a very short burst of photons emitted into a medium will take a finite amount of time to reach a detector at any arbitrary location. The time period between emission of the burst and the end of photon detection can be divided into time windows. Photons that arrive at the earlier time windows, have traveled the most linear path between source and detector, and thus have experienced the least amount of scattering events. Therefore, the time window in which a photon is placed is positively correlated with the amount of scatter experienced. Interfaces such as edges of structures are generally sites of high scatter, thus the later time windows carry edge information. TD systems analyze the time windows of the TPSF histogram to acquire a spatial reconstruction of the tissue. Although, multiple NIR wavelengths are typically used to gain detection sensitivity to the four chromophores, the sources are not continuous like those of the CW domain systems.

Since the laser diodes employed in TD systems are required to have very high repetition frequencies (typically in the order of 10 - 100 MHz), and the detection systems must have the sensitivity and processing speed to detect efficiently at these high frequencies, the components of TD systems are relatively costly. Furthermore, implementation of TD systems are far more complex than the other DOI mammography systems.

1.2.3.3 Frequency Domain

Frequency domain (FD) systems rely on the transmission of amplitude modulated light emitted by laser diodes of a specific wavelength in the NIR range to measure DC, AC, and phase of the detected signal after tissue penetration. The reason why laser diodes are used is because they can be modulated at very high frequencies. Modulation allows for the time delay between photon emission and detection to be quantified, thereby providing an avenue to distinguish scattering from absorption. The modulation frequency in FD systems is generally between 70

MHz and 1 GHz as frequencies greater than 1 GHz are dominated by noise due to insufficient modulation depth [16]. FD systems typically use laser diodes of discrete wavelengths in the NIR range such as 690 nm, 785 nm, 800 nm, and 830 nm.

In essence, measurements from FD and TD systems are Fourier transforms of each other. However, FD systems are slightly less costly than TD. FD systems are also easier to couple with fiber optics, which is not the case for TD systems as fiber length can have an effect on the TPSF used for the discrimination of optical properties. However, because FD systems are generally single wavelength instruments, they are not suited for spectroscopy like CW domain systems.

1.2.4. Diffuse Optical Tomography (DOT)

A majority of the previous studies on optical mammography have used a tomographic configuration of source and detector fibers for image reconstruction. The tomographical approach generally involves multiple stationary coupled source-detector pairs (typically 16 - 32) that interface with the breast. The source-detector pairs are situated either in a circular or parallel plate arrangement around the breast. 3D image reconstructions of optical properties and chromophore concentration are produced by applying analytical forward models based on the standard diffusion equation and inverse reconstruction procedures [7],[8],[9],[14],[15].

Although DOT produces image reconstructions that can distinguish hypoxic and non-hypoxic areas it suffers from poor spatial resolution due to the diffusivity of NIR light in breast tissue and the fact that the inverse diffuse imaging problem is ill-posed. This is demonstrated in Figure 1.2 which shows that the photon propagation pathways between a source and detector form a banana shape in breast tissue. Essentially this means that one source-detector pair acquires photons traveling through a volume of breast tissue thereby increasing voxel size in the 3D reconstructions and negatively affecting resolution.
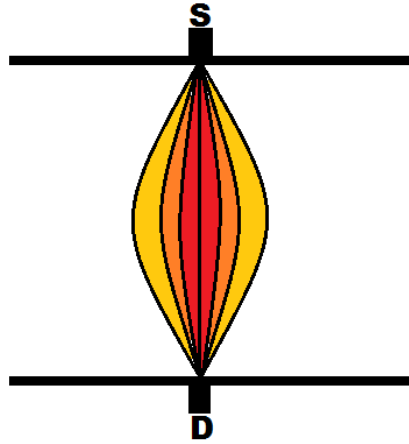
Figure 1.2. Photon propagation pathways between a source and detector in a diffusive medium such as breast tissue that are detected by the detector. Darker shades signify less scatter and therefore a higher chance of being detected than the lighter shades which signify more scatter.

A study that exemplifies this dilemma is that conducted in [15]. In their study, they distinguished between benign and malignant breast tumors through the use of *in-vivo* three-dimensional parallel-plate DOT. The feature that differentiates their DOT setup from others used in the past for similar three-dimensional breast reconstruction applications is the vast number of source-detector pairs that are available for signal acquisition. Whereas previous studies have used up to 10^3 source-detector pairs, the DOT setup of this study used in total 4 x 10^4 source-detector pairs. Theoretically, this high number of source-detector pairs should translate to higher spatial resolution.

However, contrary to what was expected, the reconstructions lacked the spatial resolution to detect relevant structural features like arterial orientation and exact location and size. Furthermore, arterial structures were not discernible at all in the reconstructions. Instead, their

reconstructions provided a spatial representation of the chromophore markers mentioned before, which was the basis behind their discrimination between healthy and non-healthy tissue.

1.2.4.1 Standard Diffusion Equation

The theoretical basis behind image reconstruction using DOT is the Boltzmann equation. The Boltzmann equation describes the propagation of a group of localized photons at a specific location within the medium at any given time. When considering turbid media such as breast tissue where μ'_s is a lot greater than μ_a, the Boltzmann equation can be further simplified to the standard diffusion equation. This only holds true, however, when the distance between the source and detector is sufficient to allow for multiple isotropic scattering events. The equation below shows the standard diffusion equation.

$$\frac{\partial U(\vec{r},t)}{\partial t} = D\nabla^2 U(\vec{r},t) - v\mu_a(\vec{r})U(\vec{r},t) + S(\vec{r},t) \tag{1.3}$$

where D is the diffusion length given by $v/3\,\mu'_s$, v is the speed of light in the medium, and $S(\vec{r},t)$ is the isotropic photon source term that is located at $\vec{r}$ at time t. Since both μ_a and μ'_s are present of the medium.

For accurate solutions to the standard diffusion equation it is vital that boundary conditions be applied based on the geometry of the sample being imaged. There are three main types of medium geometries; infinite, semi-infinite, and slab geometry. Each geometry has unique solutions to the standard diffusion equation. Infinite geometry mediums are the ideal case in which the source and detector are submerged in the medium which is infinite in all directions. The source is considered to be point like and isotropic. In contrast, the medium geometry is said to be semi-infinite when only one side of the medium is said to have a boundary which interfaces with both the source and detector. The last geometry, slab, is when both the source and detector interface with opposite boundaries of a medium. Determining the medium

geometry for a given DOI setup is important because the boundary conditions that each of the geometries apply to the standard diffusion equation result in different solutions.

1.2.5 2D Planar Scan

An alternate method that bypasses the complexity and computation time of DOT and achieves high spatial resolution is the 2D planar scan. Furthermore, the images generated by 2D Planar Scans are generally performed using CW domain systems and therefore hold the advantageous of being rich in spectroscopic information. In this approach, the breast is embedded between two plates behind which are a coupled collinear source and a detector fiber at opposite plates (Figure 1.3). To perform a scan, the source-detector configuration is scanned in tandem along a 2D image space while emitted photons are detected at a specified spatial sampling rate. The result of the scan is a 2D optical intensity projection of the image space where areas of high absorption are marked by lower intensity values.

The fact that the spatial sampling rate of the source-detector configuration can be controlled and is not restricted by the number of source-detector pairs like DOT systems allows for higher spatial resolution in the x-y plane. However, since the images that are produced are 2D projections, using this configuration alone does not provide any information in the depth direction (direction that is perpendicular to the plates). Past studies, like that conducted in [11], have attempted to solve this problem by employing offset detectors in conjunction with the collinear detector.
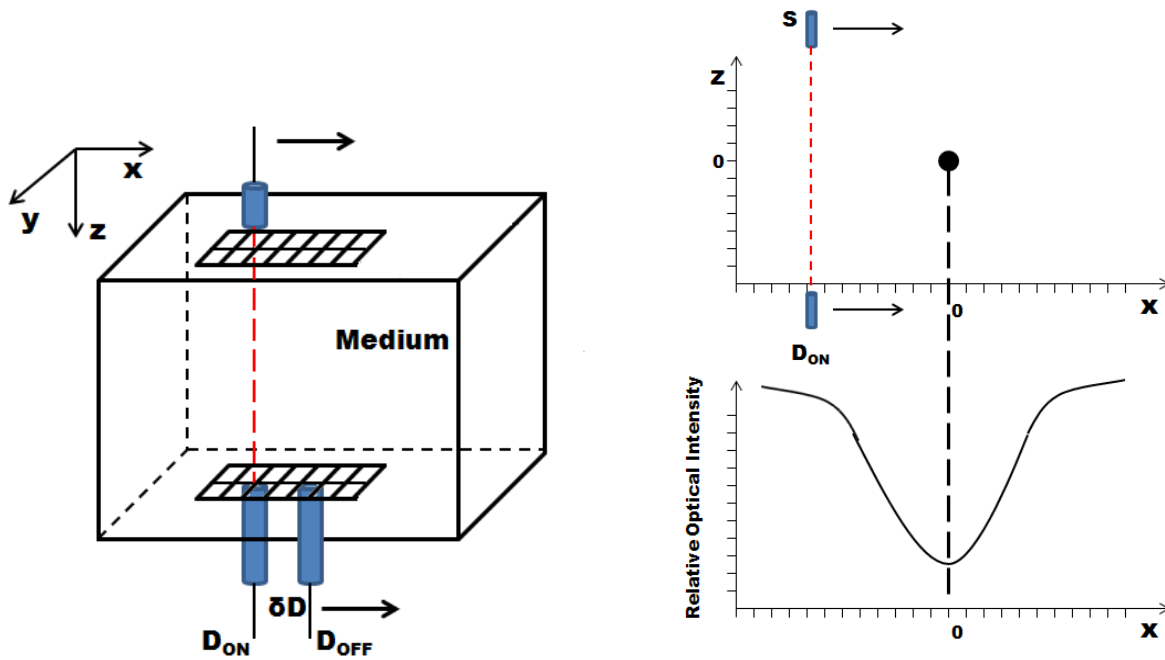
Figure 1.3. 2D planar scan source-detector configuration in both the x-y-z plane (left). The black dot in the path between the source and D_{ON} is a point like inhomogeneity. Relative optical intensity curve after a line scan of a point-like inhomogeneity at (0,0,0) (right).

In particular, [11] utilized a dual-wavelength (670 nm, 785 nm) TD scanning system with one source fiber and two detector fibers arranged in the transmission geometry shown in Figure 1.3 (left). As the figure demonstrates, the detector D_{ON} is collinear with the source while D_{OFF} is offset in the positive x direction by a specified distance, δD. For the fundamental case of a point-like inhomogeneity with an absorption coefficient greater than that of the surrounding medium, scanning the source-detector setup along the plane where the inhomogeneity resides produces an optical curve similar to that of Figure 1.3 (right). Theoretically, the negative peak of the optical curve from the collinear detector signifies the spatial location of that point-like inhomogeneity within the scanning line. The peak from the optical intensity curve produced from D_{OFF}, however, is shifted by a distance that is related to the depth of the inhomogeneity.
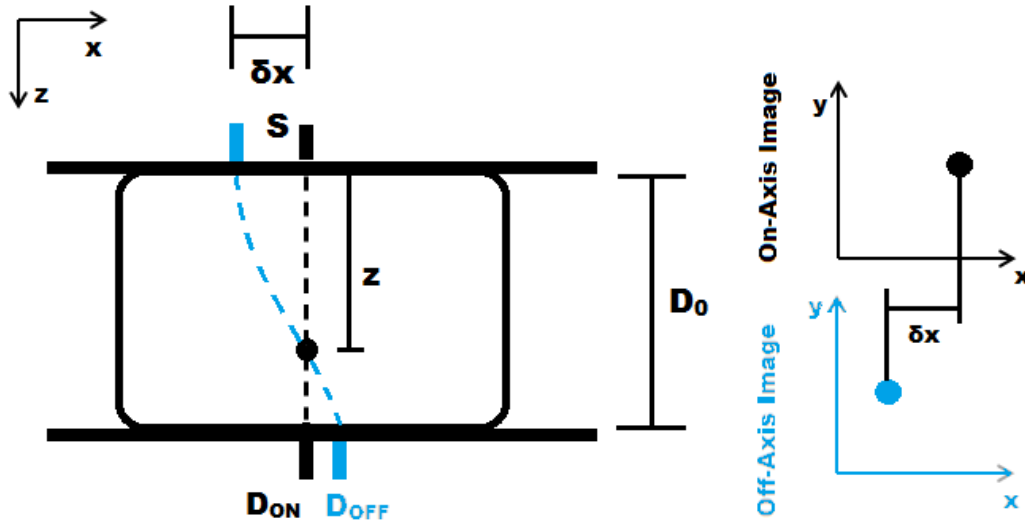
Figure 1.4. Optical sensitivity function for source-detector configuration used in [11]. The spatial location of the point-like inhomogeneity is shifted for the off-axis images due to D_{OFF} being sensitive to the inhomogeneity earlier than D_{ON}.

The rationale behind this shift is the non-linearity of the optical sensitivity function in the slab geometry as shown in Figure 1.4. As the scan traverses along the x-direction, D_{OFF} detects the point-like inhomogeneity before D_{ON}. The time interval between detection of the inhomogeneity by D_{ON} and D_{OFF} is positively correlated to the depth of the inhomogeneity. This is because as the inhomogeneity moves along the depth direction, the off axis detector becomes sensitive to the inhomogeneity sooner during the scan, whereas the on-axis detector will always detect it at the same time. In a spatial sense, this means that inhomogeneities that are deeper are shifted by a higher amount in the raw data images than those that are shallower.

Relating this shift in spatial location to depth is the foundation of the depth discrimination method used in [11]. To derive a calibration curve that relates the off-axis shift to depth, they performed Monte Carlo simulations of light propagation with a point-like inhomogeneity that

was iteratively increased in the depth direction after each simulation. The Monte Carlo simulations used the same source-detector geometry shown in Figure 1.3 (left). By taking the difference between the peak spatial location of both the on-axis and off-axis detector for each inhomogeneity depth, they were able to associate a specific off-axis shift value to a calculated depth. The resolution of the resulting calibration curve depended on the size of the depth increments in which the inhomogeneity was varied and is shown in Figure 1.5. It should be noted that they found negligible error between calculated and actual depth for different distances between source and detector.

This method provides a relatively simple and cheap means of discriminating the depth of a point-like inhomogeneity embedded in a homogeneous medium. However, there are a few drawbacks that need to be addressed before this method can be effectively used in a clinical setting. For one, it is apparent from the calibration curve that the relationship between shift and depth is not linear. In fact, the most linear portion of the calibration curve occurs in the middle depths, while the curve tends to follow a more polynomial path for shallower and deeper depths. The reasoning for this is that the reduced scattering mean free path is in the order of 1 mm and therefore distorts the banana shaped region in close proximity to the source and detectors. This essentially means that there is a higher possibility of error between the actual and calculated depths for shallower and deeper inhomogeneities since the off-axis shift is measured in discrete pixel sizes. Consequently, after they used this method to calculate the depths of carcinomas among 22 breast cancer patients, it was apparent that shallower and deeper carcinomas experienced a lot more error than those that were located in the middle of the breast tissue [11].
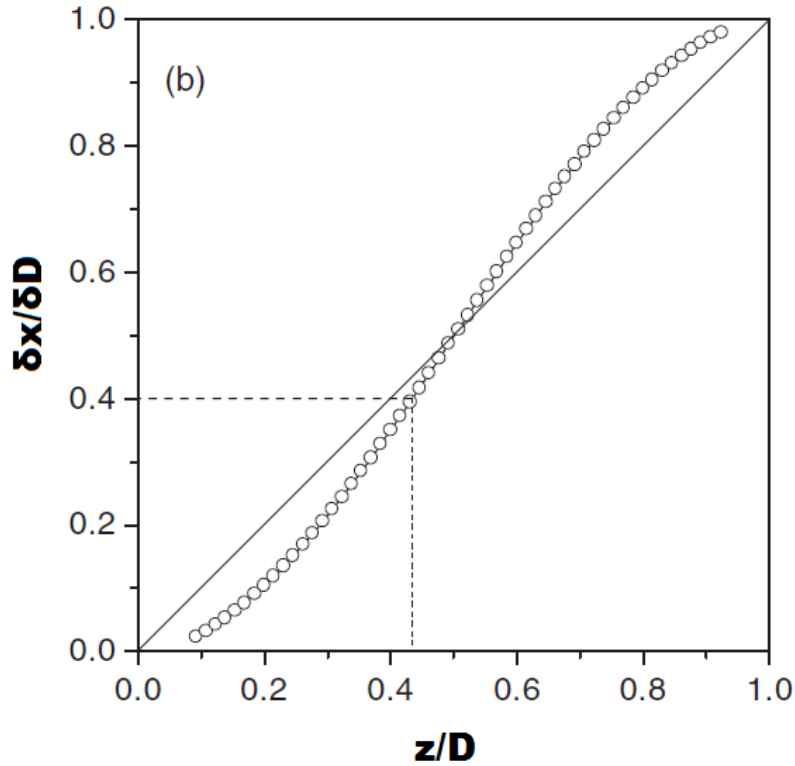
Figure 1.5. Calibration curve used in [11] to relate off-axis shift normalized to detector separation distance and depth of the inhomogeneity normalized to total depth between source and D_{ON}.

Another problem that hampers the efficacy of this method is the fact that breast tissue is not a homogenous medium and rarely are the embedded structures point-like. In fact, breast tissue is composed of networks of lymphatic vessels, veins, and arteries along with other biological molecules. Once structural units and tissue heterogeneity get more complex, it gets significantly more difficult to calculate the off-axis shifts from the 1D optical curves as there is no set protocol to associate a particular inhomogeneity in the on-axis image to its counterpart in the off-axis image.

To more effectively measure the off-axis shift experienced by a local area of an inhomogeneity such as an artery or tumor, [12] developed a method which takes into account the 2D local area centered at the pixel of interest of an obstruction in the image space. In this method, the raw optical intensity projection images are converted into binary skeletal images in which only the local peaks retain a value of "1". For each pixel which retains a "1" value, a 3 x 3 mask centered on that pixel is taken for both the on-axis and off-axis skeletal images. The off-axis mask is then iteratively shifted by one pixel to the right (or left depending on the direction of the off-axis detector), and the dot product of both the on-axis and off-axis masks is taken for each pixel shift. The off-axis mask is shifted in total by the number of pixels that equate to the separation distance between the two detectors as this is the maximum number of pixels that peak could shift by if the inhomogeneity is located in the deepest possible position. Since the dot product of the two masks increases as the skeletons line up with each other, the shift that produces the maximum dot product is therefore the shift that the pixel in question is shifted by in the off-axis image. Because it is only necessary to calculate the depths of pixels that are associated with an inhomogeneity and not the medium, a threshold is applied so that only peaks that are sufficiently deep enough to signify an inhomogeneity are conserved.

Chapter II Methods

2.1 Instrumentation

Figure 2.1 below shows the schematic of the configuration used for the experiments of this study. The main components for this configuration are a FD DOI commercial oximeter (OxiplexTS, ISS Inc., Champaign, IL) that emits and detects modulated NIR light, a liquid phantom which interfaces with the source and detector fibers of the oximeter, a microstepper to move the source-detector configuration, a computer to program the microstepper, and a computer

for data processing. The following sections will go into detail on the specifications and connectivity between each component.
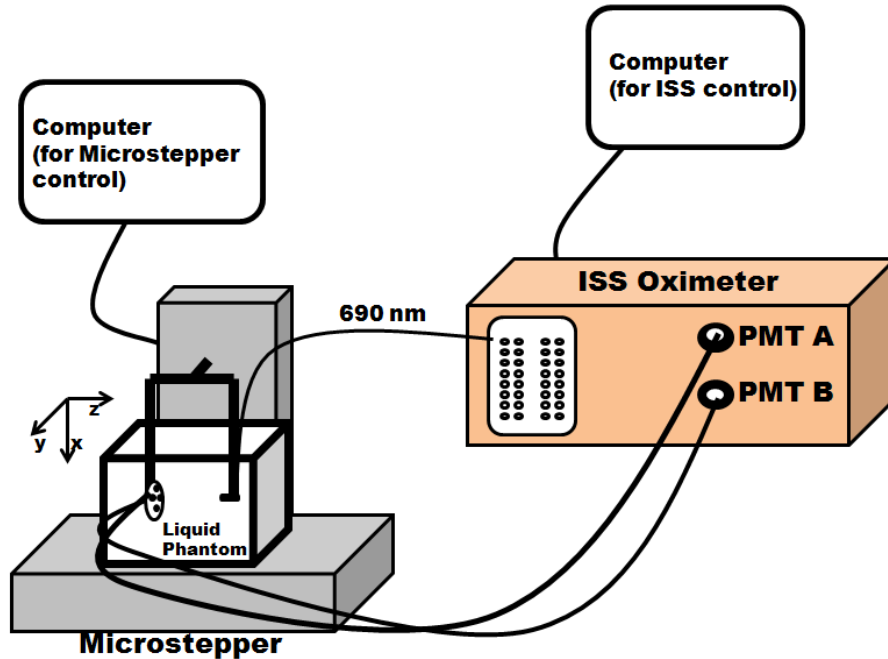

Figure 2.1. Schematic of instrumental setup used for the experiments of this study. For the scans that utilized four detectors, the scans were done twice with the detector fibers that input to the ISS Oximeter switched to those of the other two detectors.

The oximeter has 16 laser diode sources; 8 of which are 690 nm in wavelength and the other 8 of which are 830 nm in wavelength. The oximeter also houses two photomultiplier tubes (PMT) that function independently. Modulation of the light sources can be achieved by an external switch which applies a 110 MHz modulation frequency upon its activation. Laser sources of the same wavelength are sequentially switched on for a specified time interval through the use of a multiplexing circuit.

The overall result of modulation is the addition of an AC component to the illumination intensity. At the receiving end of the instrument, a heterodyne technique is applied by employing a 110MHz + 5KHz modulated signal to down convert the frequency of the detected signal to the cross-correlation frequency of 5KHz. An A/D converter then digitizes the signal which subsequently undergoes a fast Fourier Transform (FFT) to deduce the DC, AC, and phase components of the signal.

For the purposes of this study, one 690 nm light source and both PMTs were used. A 1 mm diameter optical source fiber and two 5 mm diameter detector fibers extend from the oximeter and are submerged into the liquid phantom with a configuration that will be explained later. The liquid phantom is made up of a mixture of 2% reduced fat milk and water with a volumetric ratio of 3:5 and is housed in a 20 x 25 x 40 mm^3 tank. Previous research has shown that this volumetric ratio of 2% reduced fat milk and water achieves optical properties that are similar to that which are typically found in breast tissue ($\mu_a \sim .04$ cm^{-1}, $\mu'_s \sim 7$ cm^{-1}) at a wavelength of 690 nm [12]. 3.8 gallons of the mixture were used for each experiment in this study. It should be noted that some of the earlier experiments involved a solid phantom. The reason for the solid phantom will be explained in Section 2.1.1.

In total there were two source-detector configurations for the experiments in the liquid phantom experiments of this study. As mentioned before, the source-detector configuration was attached to the platform of the microstepper. Thus, the movement of the source-detector configuration in relation to the liquid phantom medium is controlled by the microstepper. The first configuration involves an on-axis detector that is collinear to the source fiber and one off-axis detector separated in the +x direction by 15.0 ± .5 mm as shown in Figure 2.2 (left). The second configuration does not have an on-axis detector, but rather four off-axis detectors in the

+x, -x, +y, and -y directions. Each detector pair is separated by 19.3 ± .5 mm. The frame that holds the source and detector configuration was covered in black tape so as to prevent specular reflection at the frame.
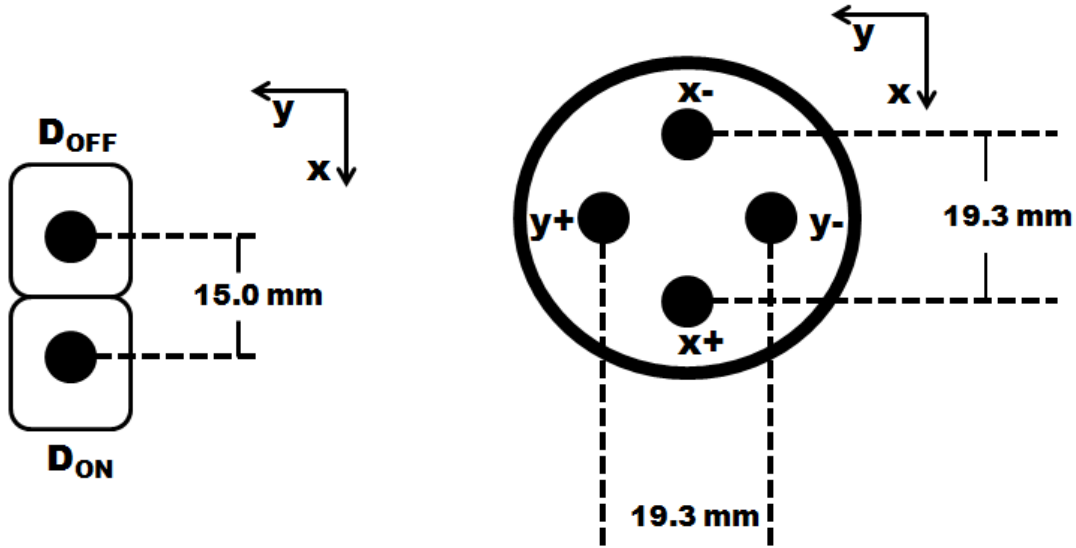

Figure 2.2.   The detector configurations used for this study.   The first configuration only involved an on-axis and off-axis detector separated by 15 mm (left).   The second configuration has all off-axis detectors in the +x, -x, +y, and -y directions, both pairs being separated by 19.3 mm (right).

As shown in the schematic of Figure 2.1, the movement of the source-detector configuration is controlled by a microstepper. The microstepper outputs a trigger signal that is directly connected to the oximeter for synchronous sampling. Also, since the source-detector configuration is setup in a sideways slab geometry, the +x direction is towards the tank floor, the +y direction is toward the front wall of the tank, and the +z direction is toward the left wall of the tank. The rods that were used as optical inhomogeneities for our experiments were placed in between the x-y plane of the source and the x-y plane of the detector. The orientation of the rod(s) depended on the purpose of the particular scan and will be explained in Chapter IV.

2.1.1 Solid Phantom vs. Liquid Phantom

Earlier in the study, a 110 mm x 110 mm x 60 mm block of delrin was used as a solid phantom with the same transmission configuration of source and detectors as Figure 2.2 (left). The Delrin block consisted of numerous drilled holes at various orientations that could be filled by either a black or white delrin rod. The diameter of the holes were less than 1 mm larger than the diameter of the rods so the rods can be fitted very tightly. The main motivation behind this phantom was to be able to scan a variety of different scenarios and rod orientations simultaneously. It was thought that when a hole did not need to be used, simply placing a delrin rod of the same make and color as the phantom would be the same as if the hole did not exist when analyzing the 2D projection images. However, the PMTs were still able to distinguish intensity peaks at the sites of the white rods. For instance, Figure 2.3. shows the optical intensity curve for a 70 mm line scan (marked in red on the phantom schematic) that was perpendicular to two parallel rods (top view) separated by ~15 mm. Even though the left rod was white, it is still detectable in the optical intensity curve.

Later we switched to the liquid phantom so we could image simple rod orientations without the data being influenced by permanent structures such as the holes of the solid phantom. Also, it was not possible to accurately deduce the exact optical properties of the solid phantom because there did not exist an adequately sized 2D space that did not encompass at least one hole. Furthermore, because the simulation software we used to derive the calibration curve operated on the basis of an infinite medium geometry, using an infinite medium geometry for our experiments should reduce the error caused by simulation discrepancies.
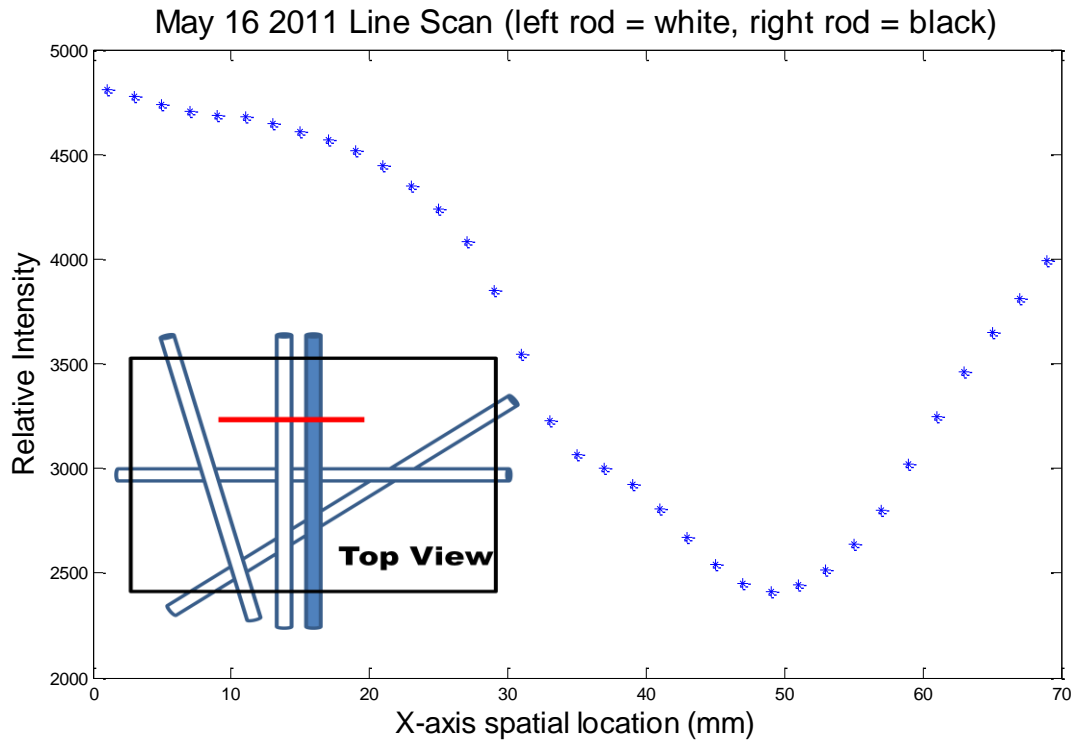
Figure 2.3. Optical intensity curve of 70 mm line scan (red) shown from the top view of the phantom. Although the left rod is white it is still detectable in the optical intensity curve.

2.1.2 Liquid Phantom Rod Holder

As shown in Figure 2.4., the rod holder used for many of the experiments consists of a circular gantry which holds a 5 mm diameter black Delrin rod through its diameter. The gantry itself is secured in a frame that is attached by a screw to the center of the tank floor. In its neutral position, the rod (and therefore the gantry) lies along the y axis of the tank approximately 6 cm above the tank floor. The screw that attaches the frame to the tank floor allows angular movement of the rod in the x-z plane. Additionally, the fact that the circular gantry can rotate about its center point allows for angular movement of the rod in the x-y plane. Therefore, this rod holder allowed for two degrees of freedom for rod orientation. Furthermore, the movements in the x-y plane can be quantified using markings for angle from 0 to 90 degrees that surround the gantry frame.

Figure 2.4 Pictures of the circular gantry used to hold the black Delrin rod. The circular gantry allows for angular movement in the x-y plane, while the frame that holds the gantry allows for angular movement in the x-z plane.

2.1.3 Four Off-Axis Detector Configuration

The four off-axis detector configuration shown in Figure 2.2 (right) was used for the liquid phantom experiments. We switched to this configuration mainly to achieve sensitivity to the direction of the rod structures. Take, for instance, the examples shown in Figure 2.5. For Case A, the rod structure runs along the y-axis in relation to the source-detector configuration. Therefore, the local gradient is at its maximum along the direction of the x-axis detectors. Likewise, the y-axis detectors are minimally sensitive to this rod arrangement because the rod runs along the same axis. In Case B, the rod is parallel to x-axis and therefore the off-axis detectors are the least sensitive to this orientation of the rod, while the y-axis detectors experience the maximum sensitivity. Theoretically, the detectors should be equally sensitive to the rod orientation in Case C because it is at 45°. Using this same rationale, the angle of a rod

structure in the x-y plane can be deduced by solving for the direction that is perpendicular to the direction of the maximum local gradient.

The four-axis detector configuration was used to test the performance (sensitivity) of the detectors when the rods were in complex positions such as angled in all three planes.
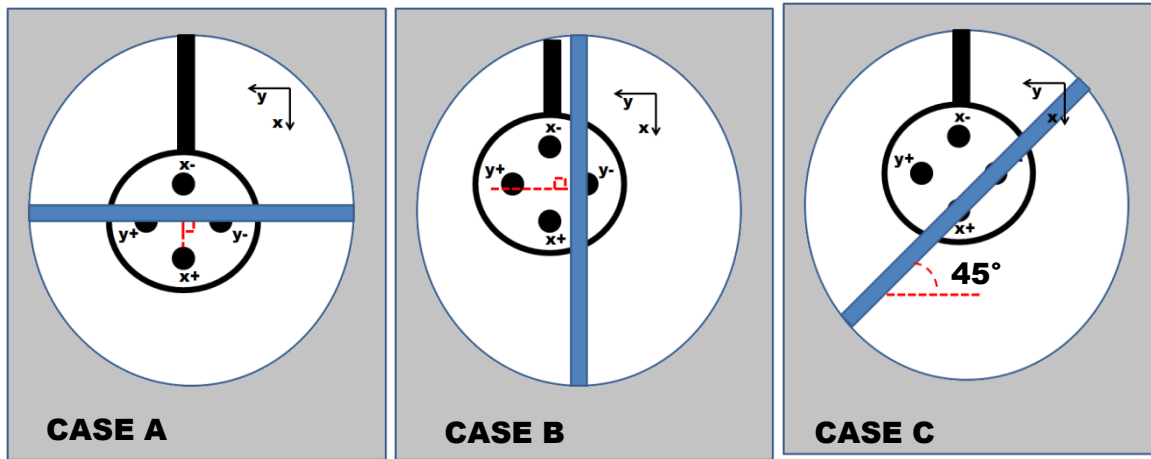

Figure 2.5 Three different cases of rod orientation (top). The x detectors are the most sensitive to the rod in Case A. Likewise, in Case B the y detectors are the most sensitive to the rod. In

Case C, both detector pairs are equally sensitive to the rod. Picture of the four off-axis detector configuration used for the experiments of this study (bottom).

2.2 Data Acquisition

Every experiment of the study scanned a 70 mm x 70 mm image space in the x-y plane of the tank holding the liquid phantom. In the first step, the microstepper sends a trigger signal to the oximeter which initiates data acquisition and scans the source-detector configuration in the +x direction for 70 mm. To achieve a spatial sampling rate of .5 mm^{-1}, the speed of the microstepper's x-axis motor is set to 10 mm/s and the sampling frequency of the oximeter is set to 5 Hz. Thus one 70 mm x-direction scan results in 36 data points (including the origin point). After the microstepper finishes traversing 70 mm in the x-direction, the oximeter stops acquiring data as it is set to wait for the next trigger signal after acquiring exactly 36 points. The microstepper then moves by 2mm in the +y direction and 70 mm in the -x direction before sending out the next trigger signal and starting the +x direction scan over again. This sequence of processes repeats until the whole 70 mm x 70 mm image space has been scanned. Therefore, each scan acquires a total of 1,296 data points (36 x 36) with each data point representing a 2 mm x 2 mm pixel.

2.2.1 Calibration Issues

To test the calibration of the microstepper motors, we tested both the distance traveled by the platform holding the source-detector configuration and the speed of the motor. The distance the platform traveled was up to .3 mm greater than the distance set by the user. This slight increase in distance can be attributed to the latency period between the driving signal to the motor and the motor physically halting motion. However, a slight increase in the distance traveled should not affect the raw data as data acquisition by the oximeter will stop after acquiring 36 points (70 mm).

In contrast, the actual speed of the motor was on average 2 mm/s faster than the speed set by the user. Unlike the previous issue, such a discrepancy in speed could greatly affect the raw data and ultimately the depth calculation. For instance, substituting 10 mm/s by 12 mm/s in Equation 2.1 leads to a spatial sampling rate of .42 mm^{-1}. This means that the oximeter will be acquiring a data point ever 2.4 mm thereby causing 2.4 mm pixel widths instead of the 2 mm pixel widths we get when the spatial sampling rate is .50 mm^{-1}. Consequently, the shift may be miscalculated as lower than its true value if 2 mm pixel widths are used for the shift distance calculation. It is apparent from the calibration curve of Figure 1.5 that an underestimated shift distance will lead to an underestimated depth calculation.

Because the motor speed was on average 2 mm/s faster than the programmed speed, we programmed the microstepper to 8 mm/s. The effective speed that was measured was close to 10 mm/s. However the operation of the timer used to measure the time it took to travel 10 mm was susceptible to human error. After ten independant trials, the error was found to be approximately $\pm$.3 mm/s.

Another issue that arose was that of scanning direction. Originally, the oximeter was set to acquire data on the microstepper's way back in the -x direction. The motivation for this was to decrease scan time as the microstepper would have to traverse through each line only once. However, the resulting raw data images experienced a stratification effect in that even numbered rows were misaligned with respect to the odd numbered rows. The cause of this stratification can be explained by the latency of x-axis motor described earlier. Although the driving signal that moves the motor is turned off after the motor has traversed 70 mm, it takes a finite amount of time for the motor to physically decelerate to a static position. In this time period, the microstepper overshoots the 70 mm mark by ~.2 mm. Therefore, the first data point that is

acquired for the next line in the y-axis is offset in the x-axis by the overshoot distance. The microstepper experiences the exact same offshoot on its way back the -x direction causing it to once again align with the x-coordinate of the previous line's first data point. In order to prevent this misalignment, the oximeter was set to acquire data only when the microstepper was moving in the +x direction. The end result was that the microstepper had to traverse each line in the image space twice, thereby increasing scanning time ~2 fold.

2.3 Data Processing

Data processing procedures were executed using MATLAB. The 5 major steps are as follows: (1) spatial processing, (2) second derivative algorithm, (3) binary image, (4) skeleton image, (5) maximum dot product. In the spatial processing step, the raw data is spatially mapped into 2D matrices and spline interpolated for higher spatial resolution. Because the main objective of the algorithm is to calculate the normalized shift between the off-axis peaks from the optical intensity curves, spline interporlated images in which the peaks of the rods were clearly distinguishable did not require further processing. For such scans it was sufficient to calculate the off-axis shift as the difference between the spatial locations (along the axis of the detectors) of both the on-axis and off-axis peaks in the optical intensity curves. The scans that required further processing were either those where the rods were in such close proximity to each other that the spatial sampling rate was not sufficient enough to distinguish the peaks. For the former case, further processing usually ended after the second derivative algorithm was applied because the resulting peaks were well-accentuated enough to clearly deduce their spatial location. However, the latter case required Steps 2, 3, and 4 because they are pre-processing steps for the maximum dot product algorithm (Step 5). The following sections go into detail about each step and issues and concerns that manifested throughout the data processing procedures.

2.3.1 Spatial Processing

The data that are acquired by the PMTs during each scan are arranged into 1D arrays. Thus it is necessary to rearrange the raw data into the spatial coordinates of the image space. This was done by arranging every 36 data points into consecutive rows. The result is a 36 x 36 pixel matrix.

1	2	3	2	1
2	4	6	4	2
3	6	9	6	3
2	4	6	4	2
1	2	3	2	1

Figure 2.6. 2D smoothing filter applied to raw data images.

Before any further data processing, the raw data is convolved with a 5 x 5 binomial smoothing filter shown in Figure 2.6. Along with reducing random noise, the application of the smoothing filter significantly enhances the performance of the second derivative algorithm by acting as a low-pass filter. It was found that increasing the size of the filter had a negligible effect on the resulting smoothed image. After this step, the image matrices were normalized to the maximum value of the raw data image and inverted.

Spatial resolution is further increased through spline interpolation, after which the resulting spatial sampling rate is 2 mm^{-1}. Therefore, the size of the images after spline interpolation is a 141 x 141 pixel matrix. Previous studies have used Monte Carlo simulations to test for possible errors due to spline interpolation, and found the variations to be below the noise level [12]. Spline interpolation resulted in smoother images where the rod structures were easily

discernible. In addition, the increased number of pixels allowed for further data processing such as the second-derivative algorithm that will be discussed in the next section. Figure 2.7 shows the raw data image of a 70 mm x 70 mm section of solid phantom with the outlines of the actual rod locations drawn in (left), and also the spline interpolated and inverted image (right) that is the result of the spatial processing step of the algorithm.
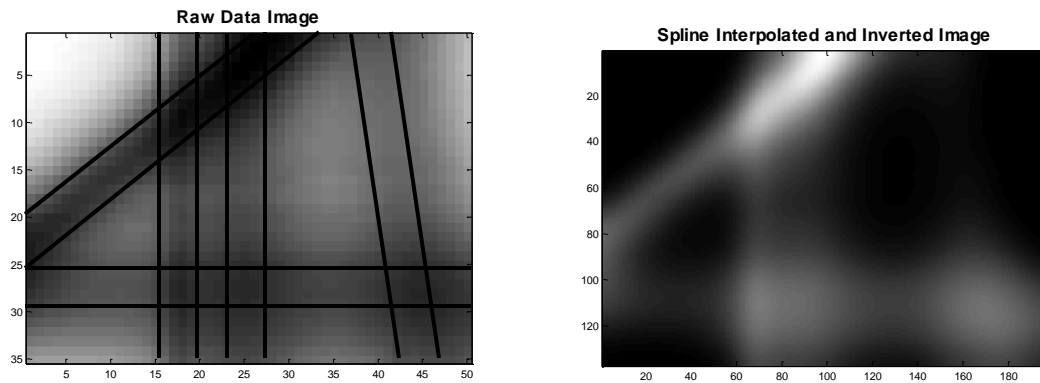
Figure 2.7 Raw data image with rod locations drawn in (left). Spline interpolated and inverted image that is the result of spatial processing.

2.3.2 Second Derivative Algorithm

As mentioned before, the second derivative algorithm was implemented to accentuate the optical intensity peaks of the spline interpolated smoothed inverted raw data (N Image). Some experiments did not require the second derivative algorithm because the rod orientations were so simple that it was easy to distinguish the spatial location of the peaks. For those that did, the second derivative was taken in four directions (horizontal, vertical, and both diagonals) using the conventional second derivative filter shown in Figure 2.8 (left). The angle of the filter was made to coincide with the direction that we wanted to apply the second derivative. Therefore, each N image produces four second derivative image matrices depending on the direction of the second derivative filter.

34
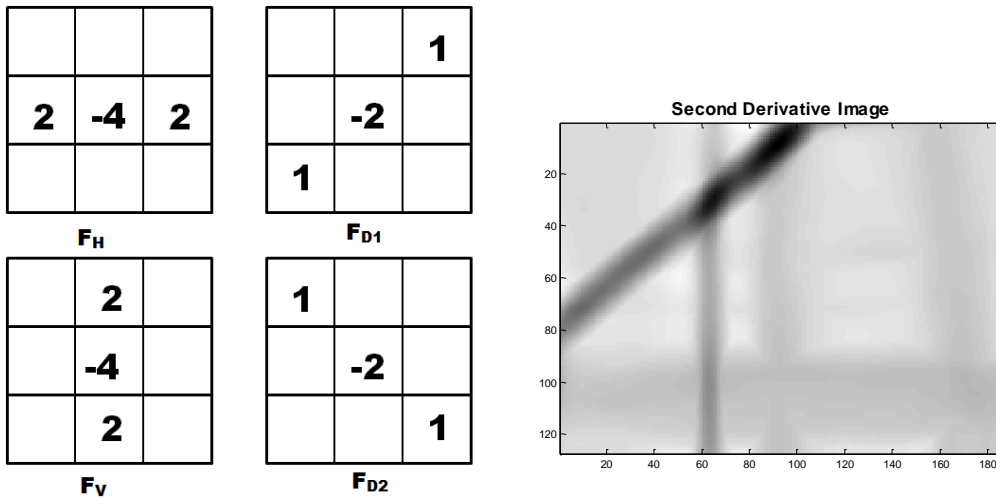
Figure 2.8 Second derivative filters in four directions used for the second derivative algorithm. The spaces between the coefficients were experimented with to see the effect on the second derivative (left). Resulting second derivative image after second derivative algorithm (right).

One of the parameters in the second derivative algorithm we experimented with was the number of pixel steps we used between each coefficient in the second derivative filter. We found that second derivative images taken with smaller pixel steps were a lot nosier, whereas those taken with larger pixel steps failed to accentuate some peaks (especially narrower peaks) in the raw data. The pixel step value of 5 was used for all experiments as it seemed to be the optimal peak value where the data was the least noisy while still preserving the inhomogeneities detected in the raw data image. In fact, 5 pixels from each side of the second derivative image are cropped because of the edge effects caused by the 5 pixel step of the second derivative filter thereby explaining the size of the second derivative matrices of 131 x 131 pixels.

After the second derive is taken for the four directions, the four resulting second derivative image matrices are then aligned on top of each other to create a 131 x 131 x 4 3D matrix. The minimum 2nd derivative value (out of the four values) are retained for each (x,y)

coordinate to create the overall 131 x 131 second derivative matrix which will be the used for further processing. The rationale for retaining the minimum second derivative is to ensure that edge information is preserved for every direction. The resulting second derivative image is shown in Figure 2.8 (right).

2.3.3 Binary Image

In order to acquire a skeleton 2D image, it is first necessary to convert the second derivative images to binary images by applying a threshold. Pixel values above the threshold are set to "0" as they represent less relevant second derivative information, while those below are set to "1" as they may suggest the location of an obstruction such as a rod. Therefore, the threshold value is an extremely important parameter when it comes to the quality of the binary images. We found that as long as the threshold was set to be more negative than the negative peaks due to noise we retain much of the rods in the resulting binary image. However, thresholding did remove some areas that were known to part of the rod as shown in Figure 2.9.
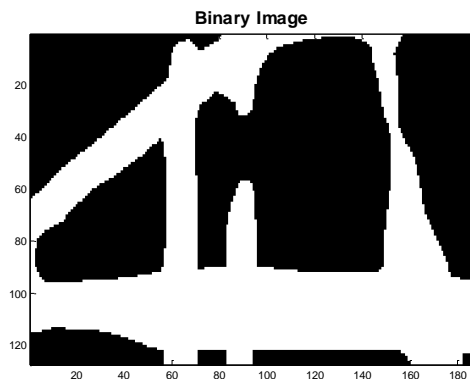
Figure 2.9 Resulting binary image. As can be seen by the gap in one of the rods, the threshold may get rid of some parts of the structures.

2.3.4 Skeleton Image

We use the bwmorph (BW2 = bwmorph(BW,operation)) function in MATLAB to convert the binary image to a skeleton image where the only values that are retained are the peaks of the optical curves. In order to achieve this, the bwmorph function utilizes image morphology. In particular, the function segregates the obstructions (which are represented as ones) of the binary image into objects. It then iteratively removes pixels from the opposite borders of the objects until no further pixel can be removed before the object breaks apart.
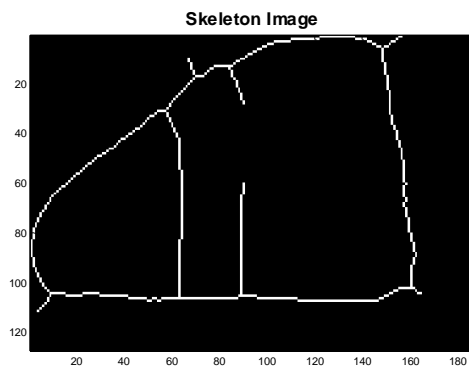
Figure 2.10 Resulting skeleton image.

2.4 Calibration Curve

The software used to derive the calibration curves which associates the off-axis shift to depth was the Diffusion&Perturbation (D&P) software (LiPTuM Lab, University of Florence, Florence, Italy). Figure 2.11 below shows the settings interface for a typical simulation.

Essentially, the D&P software allows the user to specify certain parameters about the medium as well as the spatial location of a point-like inhomogeneity within the medium in order to derive optical intensity graphs for a specified line scan with a specified source-detector configuration. The Output, Domain, and Display parameters were kept constant throughout the simulations as Fluence Rate, CW Domain, and Inhomogeneity map, respectively. However,

geometry was switched from infinite and slab depending on which phantom we wanted to derive the calibration curve for.
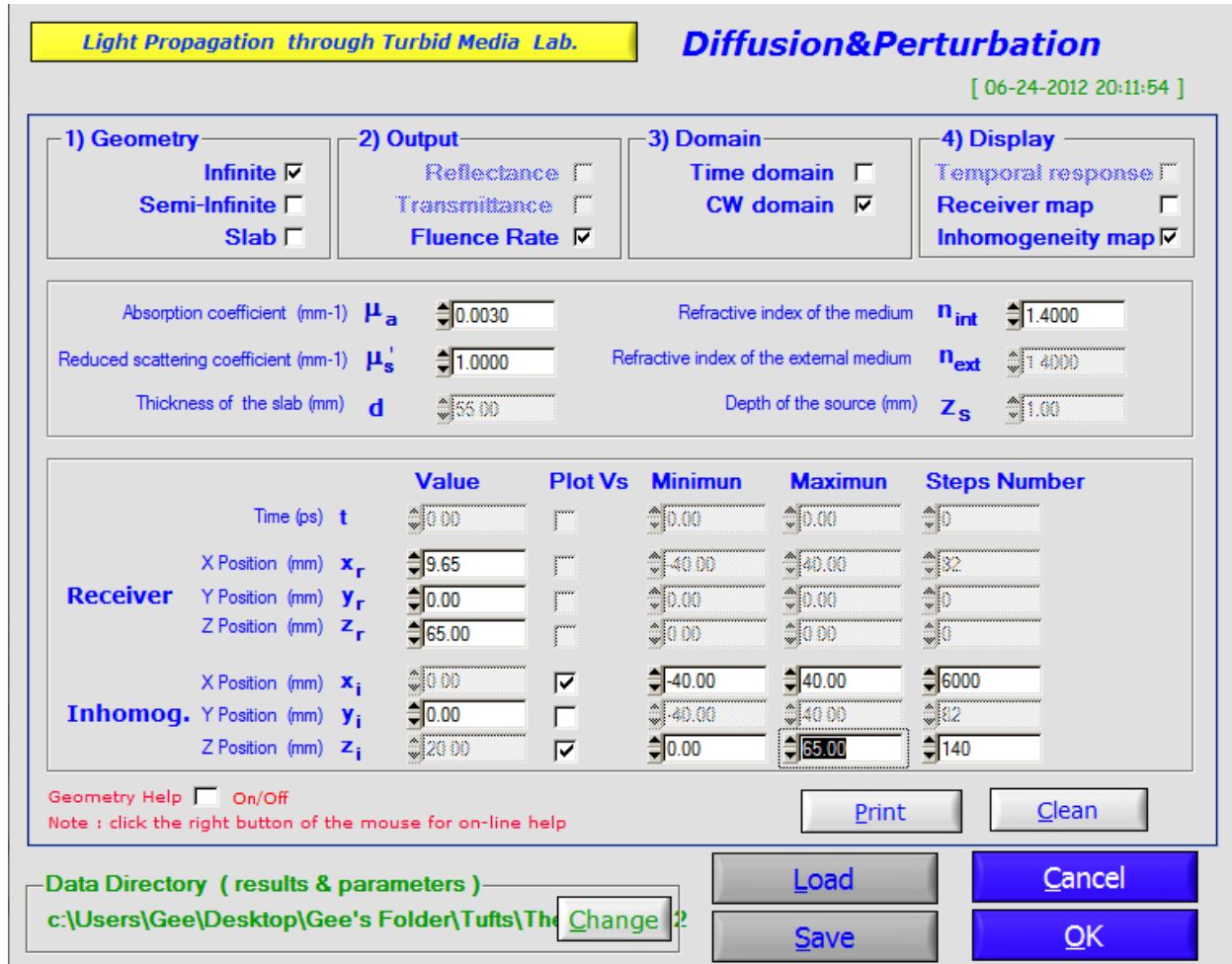
Figure 2.11 Settings interface for Diffusion&Perturbation software used to derive the optical intensity curves for a point-like inhomogeneity at a range of depths.

With these fundamental parameters set, the D&P software allows the user to specify other parameters such as the optical properties of the medium, thickness of the slab (slab geometry), refractive indices of the medium and external medium, and the depth of the isotropic source. Many of these parameters (such as slab thickness, external refractive index, and isotropic source depth) are only available if the geometry is set to slab. The refractive index of the medium was

kept at 1.4 for all the simulations. After this section (middle) of the parameter settings have been set, the D&P software further allows the user to specify the starting spatial location of the source and detector in relation to the medium, as well as the spatial location of the point-like inhomogeneity in relation to the source and detector at the start of the line scan.

Unlike the 2D planar scanning method used in this study, the D&P software does not derive optical intensity curves by moving the source detector configuration in relation to the inhomogeneity. Instead, it fixes the coordinates of the source and detector to user-specified points in the 3D space and solves forward analytical models of light propagation between the source and detector in relation to the spatial location of the inhomogeneity. Therefore, to perform a line scan, we kept the y-coordinate of the inhomogeneity at 0 and varied the x-coordinate of the inhomogeneity from -40 to 40 in 6,000 steps. In effect, this is the same as if the inhomogeneity was kept at x = 0, y = 0 and the source-detector configuration was scanned from x = -40 to 40 with a sampling rate of 75 Hz. This same line scan was performed for a user-specified range of depths for the inhomogeneity which encompassed the total distance between source and detector in 140 steps.

Therefore, the output .csv file from the simulation includes a 140 x 6000 element matrix. Each row represents the optical intensity curve for the 80 mm x-axis line scan when the inhomogeneity is at a particular depth. Since we want the optical intensity curves for a detector pair (in each direction for the second source-detector configuration in Figure 2.2), each calibration curve required two simulations; one for each spatial location of the detector. Using Matlab, for each depth we found the spatial location of the peaks in the intensity curves from each detector of the detector pair. The difference between these two spatial locations for a particular depth normalized to the detector separation distance is our normalized off-axis shift

that corresponds to that depth. Through this method we are able to derive off-axis shifts throughout the remainder of the range of depths between source and detector. Since some experiments used different source-detector separation distances, we had to sometimes repeat the scans with the altered value.

A key issue that should be noted is that of the resolution of the spatial location range of the inhomogeneity. The x-axis resolution limits the off-axis shift to a particular increment. However, since the resolution in the x-axis for these simulations were essentially 75 mm^{-1}, the off-shift can be calculated precisely (within .001 mm) for a particular depth. However, since the depth (z-axis) resolution is significantly smaller, this significantly limits the resolution of the calibration curve. For that reason, some calibration curves may have depth values that are associated with a range of off-axis shifts.

Chapter III Experiments & Protocols

3.1 Calibration Curve Simulations

3.1.1 Optical Property Variation

A subject of much interest was how different optical properties would affect the calibration curve. This is especially important when dealing with breast tissue, as breast tissue is an inhomogeneous medium and therefore exhibits a range of optical properties instead of a fixed value. According to [13], at 670 nm the average μ_a and μ'_s are .0036 ± .0008 mm^{-1} and 1.05 ± .13 mm^{-1}, respectively. Therefore, if variations in the optical properties of the medium result in different calibration curves, this could cause significant error in calculated depth since the optical properties used in the D&P software may not correspond to those of the scanned medium. The only way to solve this issue would be to perform an initial scan to calculate the bulk optical properties of the tissue/phantom and inputting these optical properties to the D&P software.

To test the variance of the calibration curve due to discrepancies between real and simulated optical properties, we performed simulations for a range of optical properties. For μ_a we chose values of .001, .003, and .005 mm^{-1} and for μ'_s we chose values of .5, .72, 1.0, and 1.5 mm^{-1}. We deliberately chose extreme minimums and maximums for both optical properties with the thought that if the calibration curve does not experience a significant amount of variation between such a high range, then this would mean there should be even less variation for the optical property range actually found in breast tissue. For these simulations we set the depth of the detector in relation to the source to 55 mm and the offset distance of the off-axis detector was set to 15 mm.

3.1.2 Off-Axis Detector Distance

Another parameter from the D&P software that was of interest was the off-axis distance, δD. [11] has reported that as δD is increased, the depth resolution increases as well. For their study, however, they used a δD of 10 mm. Their justification for not increasing δD even further was that the increase in separation between the two detectors may cause edge artifacts because one of the detectors could possibly surpass the edge of the sample during the scan. In contrast, the δD used in [12] was 20 mm. Their claim was that the normalized shifts are independent of the offset distance.

We performed simulations in the D&P software with the off-axis detector offset by 5, 10, 15, 20 and 25 mm in relation to the on-axis detector. We chose three different pairs of optical properties for the medium; (1) $\mu_a = .001$ mm^{-1}, $\mu'_s = .5$ mm^{-1} (2) $\mu_a = .001$ mm^{-1}, $\mu'_s = 1.5$ mm^{-1} (3) $\mu_a = .005$ mm^{-1}, $\mu'_s = .5$ mm^{-1}.

3.1.3 Source x-y position

Another concern was the spatial location of the source fiber in the x-y plane with relation to the off-axis detector(s). This is not so much of a concern with the first source-detector configuration as it is relatively simple to check the collinearity of the source fiber and on-axis detector. To do this, we acquired data with the first source-detector configuration at a static location and a filter between the source and detector fibers so as not to oversaturate the PMT. We then moved the source fiber by hand and secured it at the location which caused approximately the highest intensity peak in the real time data acquisition feed on the computer monitor from the on-axis detector. Once this peak was achieved in the acquired data, the detector was said to be on-axis and secured to that exact location.

However, the second source-detector configuration does not have an on-axis detector to use as a reference. Therefore, it is extremely difficult to secure the source fiber by hand so that its spatial location in the x-y plane is at the midpoint of both detector pairs. It is for this reason that we investigated just how important it was for the source to be exactly at the midpoint of the four off-axis detectors. If differences in the source location do not cause significant differences between the calibration curve, this will translate to less time required in the experimental setup to accurately position the source fiber. For our simulations, we first investigated four cases of source position in the x-y plane (Figure 3.1). Case A is when the source is offset by 5 mm before the -x detector. Case B is when the source is exactly on top of the -x detector. Case C is when the source is offset by 5 mm after the -x detector. Lastly, Case D is when the source is exactly at the midpoint between all detectors. We only performed simulations for these four cases, because we believed that the characterization of error due to these changes in source location in the x-y plane should be symmetric about both the x and y axis.
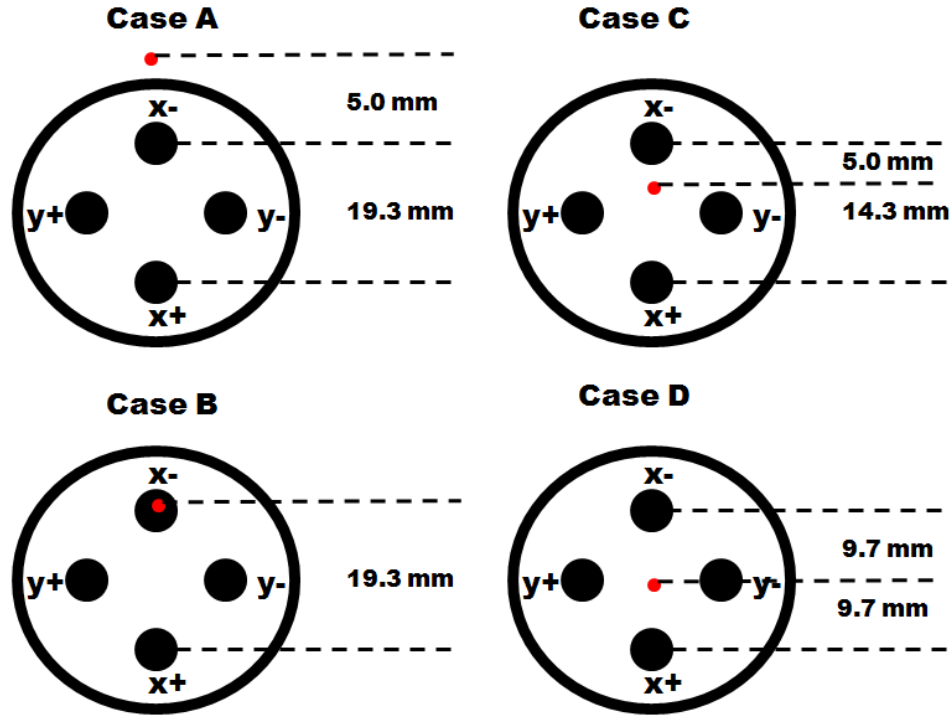
Figure 3.1 The cases which varied source position along the x-axis. The source positions were chosen in relation the x⁻ detector. The law of symmetry can be used to apply the same calibration curves for the other detectors.

A more complex variant of the four cases is when the source is not positioned on either the x or y axis. For cases E to H, the source position was offset in the x and y axis. Specifically, we wanted to see how the calibration curves would react to increasing distance in the y direction between the source and the x detector pair. The calibration curves derived for Case E to H were compared to that of Case D in which the source is located at the midpoint between the x detector pair. If increasing the distance isotropically from the midpoint does cause an error between the calibration curves, then it is important that we quantify a maximum source offset radius in relation to the midpoint between the detector pairs in which the error is negligible. In fact, this

offset radius dictated how accurate we had to be when positioning the source in relation to the detectors in the x-y plane. Figure 3.2 shows the source position for Cases D through I.
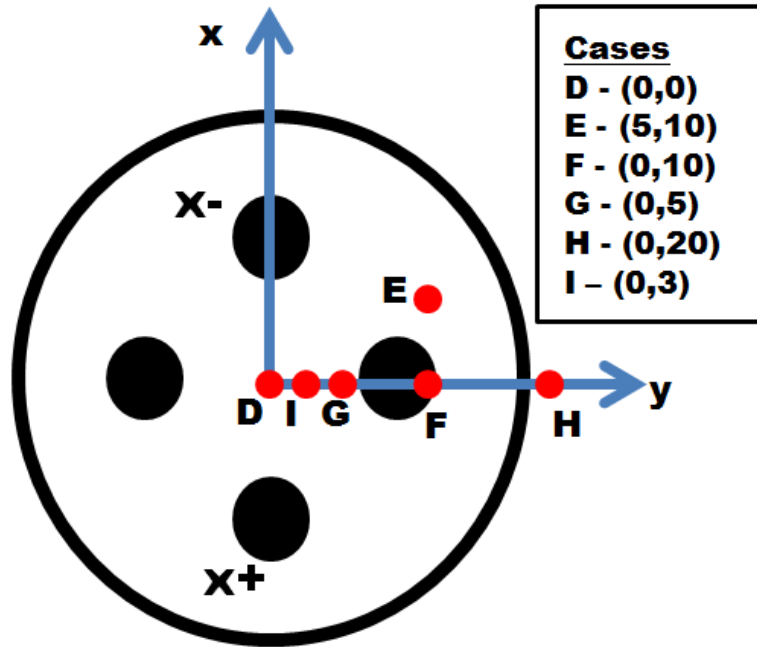
Figure 3.2 Cases D through I that test for source detector variation in the y direction and both x and y direction (Case E).

3.1.4 Infinite vs. Slab Geometry

Since we used both a solid and liquid phantom, it was important that we assess the effect of the medium geometry on the calibration curves. For the liquid phantom, the geometry was set to infinite like the previous simulations. However, to take into account the boundaries of the solid phantom, the geometry for the solid phantom simulations were set to slab. As mentioned before, when the slab geometry is selected in the D&P interface, the software allows the user to set two more parameters that were not selectable for the infinite geometry; the refractive index of the external medium (n_{ext}) and the effective depth of the source (Z_s). n_{ext} was set to 1.4 like the refractive index of the internal medium (n_{int}). Because the medium has a slab geometry, the

spatial location of the source is not isotropic. Instead, the spatial location of the effective isotropic source is calculated as $1/\mu'_s$, or Z_s. Hence, for the optical properties used for both the infinite and slab geometry simulations ($\mu_a = .001$ mm^{-1}, $\mu'_s = 1.5$ mm^{-1}), Z_s was set to .67 mm (1/1.5).

3.2 Fundamental Experimental Protocol

Every scan that was performed in this study followed a specific protocol to reduce any sources of error or other factors that may influence results.

Firstly, the oximeter was switched on along with the PMTs to warm them up before performing the scans. A lot of care was taken in turning the gain of the PMTs to their lowest setting so as to not oversaturate the PMTs when they are turned on. We left them on for ~45 minutes which was the time that the manual from ISS recommended. Then we jogged the microstepper (and therefore the source-detector configuration) to its starting location for the scan. This starting location varied depending on which phantom we were scanning and the spatial area we wanted to scan.

3.3 Liquid Phantom Scans

The liquid phantom scans gave us more freedom when it came to rod arrangement and orientation because we did not have to deal with predefined holes like the solid phantom. Additionally, the rod holder (Figure 2.4) allows us to alter the orientation of the black rod in a quantifiable manner. We used the four off-axis detector configuration shown in Figure 2.2. In this source-detector configuration, the off-axis detectors are offset in the +x, -x, +y, and -y directions by $9.7 \pm .5$ mm.

As mentioned before, the premise of the liquid phantom experiments was to test the depth discrimination method presented in [11] and [12] for the simplest rod orientations. This

could not be achieved by the solid phantom because the holes were still detectable by the PMTs even when they were filled with white rods. Therefore, it was very difficult to find a 2D area within the solid phantom that did not include intersecting rods which may affect data analysis. By using the liquid phantom, we can be sure that the intensity values are not being influenced by anything other than the liquid medium and the rods we submerge in it.

We started off with the simplest structural arrangement of one rod with which we performed experiments for three cases. In the first case, the rod is kept at constant depth (z-axis) throughout its length and runs along the y-axis. For the second case, the rod was still kept at a constant depth, however, it was angled in the x-y plane. Likewise, for the third case, the rod was angled in the y-z plane as well. The objective of these three experiments was to characterize the performance of all four off-axis detectors for different structural orientations of one rod. The chief criteria we used to rate the performance of the detector pairs was the error between the calculated and actual depth. Since the D&P program we used to derive the calibration curves considered a point-like inhomogeneity, we expect to experience some type of error because the inhomogeneities we are using for the experiments are rods. Therefore, the error experienced in Case I, which is the simplest arrangement of the rod in relation to the source-detector configuration, will be our reference point in which we will compare the errors of the other cases to. This is because the error experienced by the Case I should have more to do with the discrepancy between geometries of the actual phantom and the simulation medium rather than that due to orientation.

The fourth case was performed on two rod arrangements in which another rod was added to the image space by securing it to the front and back walls of the tank. The two rods were arranged so that they would intersect in the x-y plane. More specifically, the first scan was when

the rod attached to the gantry was kept parallel to the y-axis while the rod that was secured to the walls was kept at angle in the x-y plane , and the second scan was when both rods were angled in the x-y plane with the angle between the rods ~45°. All the experiments will be further explained in later sections.

3.3.1 Liquid Phantom Protocol

There were some additions to the basic experimental protocol that was discussed in Section 3.2 for the liquid phantom scans. For one, since four off-axis detectors are used for these scans, each scan had to be performed twice as the oximeter has only two PMTs. Therefore, for each case, the first scan was performed with the x detector fibers connected to the PMTs, while the second scan was performed when the y detector fibers were connected. For the first time we ran the Case I scans, the scan direction was kept along the x-axis for both x and y detector scans. However, we started to alternate the scan direction to the direction of the detector pairs we used. Therefore, before we performed the scan with the y detector pair, we switched the scan direction to the y-axis. Essentially this means that instead of the detectors traversing back and forth in the x direction by 70 mm and moving up 2 mm in y direction after each iteration, the opposite will be accomplished. The reasoning behind this change in scan direction is the non-smooth quality of the y-axis lines of the image which made it difficult to accurately calculate the spatial location of the inhomogeniety peaks in the images.

Another addition to the fundamental experimental protocol is the fact that we had to measure the spatial location of the rod(s) before each scan was performed. This did not have to be done for the solid phantom because the holes in which the rods fill were predefined, thus their spatial locations were already known. With the rod (in the rod holder) fixed into a specified orientation, we used the microstepper to position the source-detector configuration so that the rod

would attain the spatial location we desired for a particular experiment. For the simplest case of a rod along the y-axis, to achieve a specific depth we would first position the source fiber tip directly on top of the center line of the rod. Then we would move the source-detector configuration along the z-axis by the depth we wanted the rod to achieve. This was done for both the first and last point of the rod that was in the image space to make sure that the rod was in fact parallel to the y-axis. A similar process was used for rods of angled orientations.

Because the main objective of this study was depth discrimination, we were more lenient when it came to the x and y locations of the rods. Our main concern was to have as much of the rod(s) in the center of the image space as possible. This is so that we can maximize the number of rows (columns) where the optical intensity peaks caused by the rod(s) are clearly visible for both detectors in each detector pair. For some cases that involved rods angled in the x-y plane, we only considered the rows (columns) where the peaks from both detectors were clearly distinguishable on the optical intensity curves.

Once the rod(s) was arranged to its specific position for the experiment, we began the process of reducing as much peripheral noise as possible. The main measures that were taken were to shut off all the lights in the room, dim the computer screens (after compiling the program microstepper program), and covering the tank with a black cloth.

During the scans, we were conscientious to make sure that the initiation and termination of data acquisition by the oximeter coincided with the beginning and ending of each traversed line by the source-detector configuration.

3.3.2 Liquid phantom noise characterization

An ideal liquid phantom would be one that exhibits an infinite geometry with the exact optical properties as those that were used to derive the calibration curve. Practically speaking, achieving an ideal infinite medium geometry where the medium expands in all three directions to infinity is not possible. The only solution is to construct a phantom whose dimensions are sufficient enough to effectively imitate an infinite medium geometry. For this study, one of the major issues during the construction of the liquid phantom was building it with dimensions that made it effectively infinite while still having it not restrict the range of movement of the microstepper platform that is directly behind. Such a task proved to be difficult because of the limited area of the microstepper stage where the liquid phantom was situated. In the end, it was decided to use the liquid phantom presented in Section 2.1.

As described in Section 2.2, for a scan performed for the x detector pair, the source-detector configuration is traversed through the x-axis (axis perpendicular to the floor of the tank) for 70 mm, and then moved incrementally in the y direction by 2 mm. Because the total distance the source-detector configuration travels in the y-axis is 70 mm as well, the three dimensional image space is a 70 mm x 70 mm x 55 mm box (for a source-detector separation distance of 55 mm). Therefore, since the length of the tank which holds the liquid phantom is 110 mm, a major concern was the effect of the tank walls on the data images. It is expected that because the walls of the tank are built from black PVC, any photons that do propagate to the border have a high probability of being absorbed resulting in a lower intensity counts at the top and bottom edge of the image. It is also expected that photons will be lost in the left edge of the image because of the liquid-air interface. Even with these reductions in intensity, absorption by the tank walls is more desirable than if they were highly scattering as scattered photons still have the possibility

of being detected by the detector fiber. Because the source and detectors were both away from the side walls by ~6 cm each, these walls were not of concern.

Another parameter that can affect instrumental noise are the gain settings of the PMTs. Two knobs in the oximeter interface were used to control the gain of the PMTs during each experiment. These knobs directly control the number of photon counts that can pass through the orifice between the PMT and detector fiber. Typically, a desirable gain would result in a noise-to-signal ratio (NSR) that is ~.01.

Thus to characterize the instrumental noise, we performed line scans in the x direction of the tank for different y coordinates and different gain settings with the tank just filled with the water-milk mixture. Since the gain value varied when the liquid phantom was replaced, it was more advantageous to vary the gain by the DC photon count we saw on the oximeter software interface. Thus, the gain settings were switched from a "High" gain value and a "Low" gain value. The "High" gain value was the value in the knob that lead to an average DC photon count of ~14,000 ± 1000. In contrast, the "Low" gain value was that which lead to an average DC photon count of ~1,200 ± 100. For some experiments, 30 ml of Indian Ink were added. For these experiments, the "High" and "Low" values were the values that lead to an average photon count of ~4,200 ± 200.
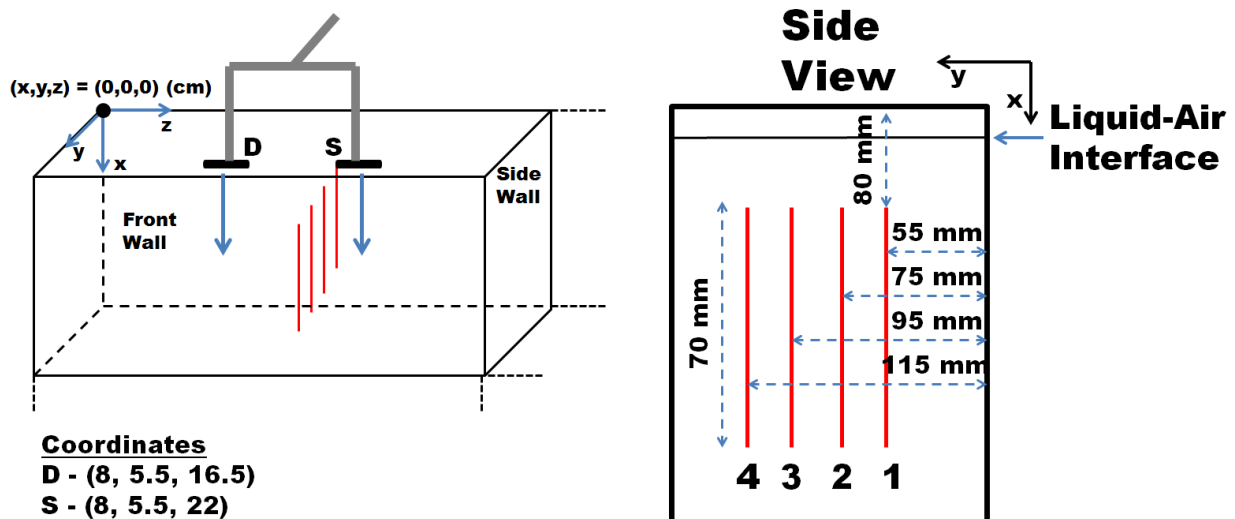
Figure 3.3 Schematic of scans for noise experiment. To avoid confusion, the axis directions were chosen as the same directions as the resulting image. All coordinates are shown in relation to the origin point which is the top left corner of the back wall.

It should be noted that for the noise experiments, we used a static motor scanning method. Unlike the continuous scan which we used for the other experiments, in this method the source-detector configuration does not traverse continuously through each line. Rather, it halts at each sampling location every 2 mm throughout the line and acquires 30 samples. Therefore, with the sampling rate of the oximeter kept at 5 Hz, the microstepper was programmed to remain at each location for 6 seconds. Since the line scans are 70 mm, this accounts for 1,080 samples for each line. Figure 3.3 shows the scans that were performed for this experiment. As it shows, the line scan was performed 5.5, 7.5, 9.5, and 11.5 cm from the back wall. Because we were not trying to discriminate the depth of an inhomogeneity, only the on-axis detector of the first source-detector configuration (Figure 2.2) was used. Also, after performing the scans with the liquid phantom unaltered, we repeated the scans with the addition of 30 ml of Diluted Higgins India Ink (UniFi) to the μ_a of the water-milk mixture. We did this to investigate if the noise characteristics could be noticeably improved by preventing the detection of scattered photons by the PMTs.

3.3.3 Case I

For this case, the rod was arranged parallel to the y-axis and at a constant depth. We experimented with a total of six depths (10, 20, 30, 38, 40, 50, and 55 mm). This range of depths was chosen because they comprised much of the range of the total source-detector distance of 65 mm. The main objective of this experiment was to see how the error between the calculated and

actual depth responded at different depths. As mentioned in Section 1.2.5, we expect the error to be higher for shallower and deeper depths (by ~7 mm) due to the steepness of the calibration curve at these depths.
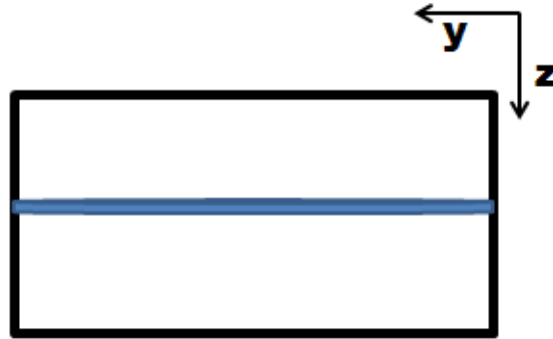
Figure 3.4 Orientation of rod for Case I.

3.3.4 Case II

This experiment involved rods at a constant depth like Case I, however the rods were angled in the x-y plane. The depth of the rod was kept at $32.8 \pm .3$mm. The rod angles which were chosen for this experiment were $0°, 20°, 35°, 45°, 55°, 70°, 90°$ in relation to the x-axis. As mentioned before, the first time we performed the scans on this experiment the scan direction was along the x-axis. Later we repeated this experiment and changed the scan direction to the y-axis for the y detector scans.

The main objective of this experiment was to see how angling the rods in the x-y plane would affect intensity peak location between the off-axis detectors. In particular, we were looking to see if the broadening of the peaks as the angle between the detector pair direction and the rod decreased (to make it less perpendicular to the scan direction) caused an increasing trend to the error.
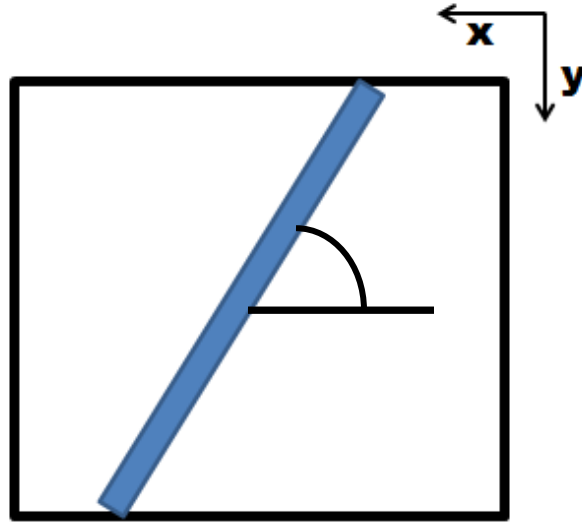
Figure 3.5 Orientation of rod for Case II. The angle shown in the figure is varied from 0 to 90°.

3.3.5 Case III

For Case III, the rod was kept parallel to the y-axis like Case I, except this time the rod varied along depth direction (y-z plane). The angles that were chosen were not quantified but were recorded in relation to one another. When looking at the y-z plane, Angle 1 was the smallest angle between the y-axis and the rod and every successive angle was increased by ~15°. Separate x detector and y detector scans were taken for this experiment as well with the same switching of scan direction depending on the detector pair being used.

The premise behind this experiment was to see how error is affected by the fact that the rods are angled in the depth direction.
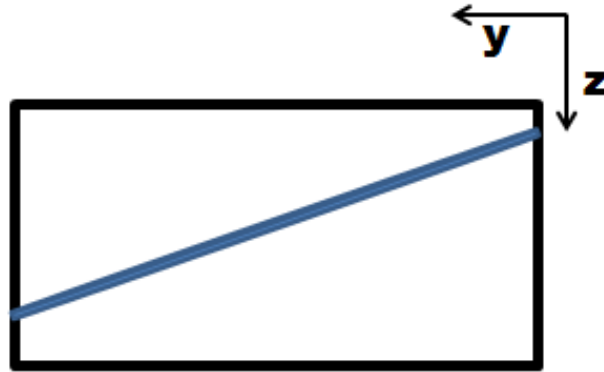
Figure 3.6 Orientation of rod for Case III.

3.3.6 Case IV

Case IV is the first case in which we use two rods. For the first scan, the rod on the circular gantry was kept at a constant depth and parallel to the y axis while the second rod was kept at one arbitrary angle. In the second scan, the rod on the circular gantry was kept at an arbitrary angle as well. The purpose of this experiment was to qualitatively characterize the effect of overlapping structures to the results.
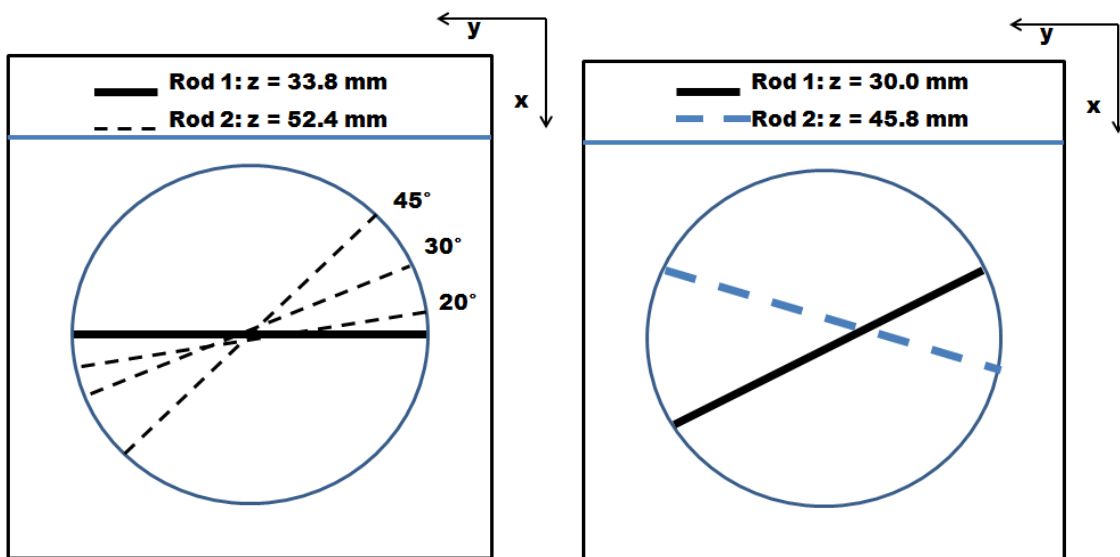
Figure 3.7 Schematic of rod orientations used for Case IV.

Chapter IV Results

4.1 Calibration Curve Results

4.1.1 Optical Property Variation

Figure 2.6 shows the four calibration curves along with error graphs to show the error between the extremes of μ_a with μ'_s kept constant and vice versa. The first error graph of Figure 2.6 shows the error between off-axis shifts for when the simulations differed in μ_a. Likewise, the second error graph shows the error for when the simulations differed in μ'_s. It is apparent that the error follows the same trend for both optical properties. They both experience more error for shallower and deeper depths. More specifically, the peaks in the error graphs occur for normalized depths from ~.15 to .35 and ~.6 to.85. In contrast, the middle depths (z/D ~ .4 to .6) as well as depths in both the shallowest and deepest depths experience the least amount of error. However, even though this trend in error exists, the maximum error from both graphs is only .04. In terms of distance, a normalized shift of .04 accounts for .6 mm when the off-axis detector is offset by 15 mm. When compared to the spline interpolated images described in Section 2.4a, this is approximately this size of one pixel. Therefore, we safely concluded that the variance of breast tissue optical properties will have a negligible effect on the calibration curve. Since both the Delrin solid phantom and the water-milk medium of the liquid phantom are highly scattering mediums, we set μ'_s to 1.5 mm^{-1} and μ_a to .001 mm^{-1} to derive the calibration curves used in our experiments.

Sc = .50 mm-1
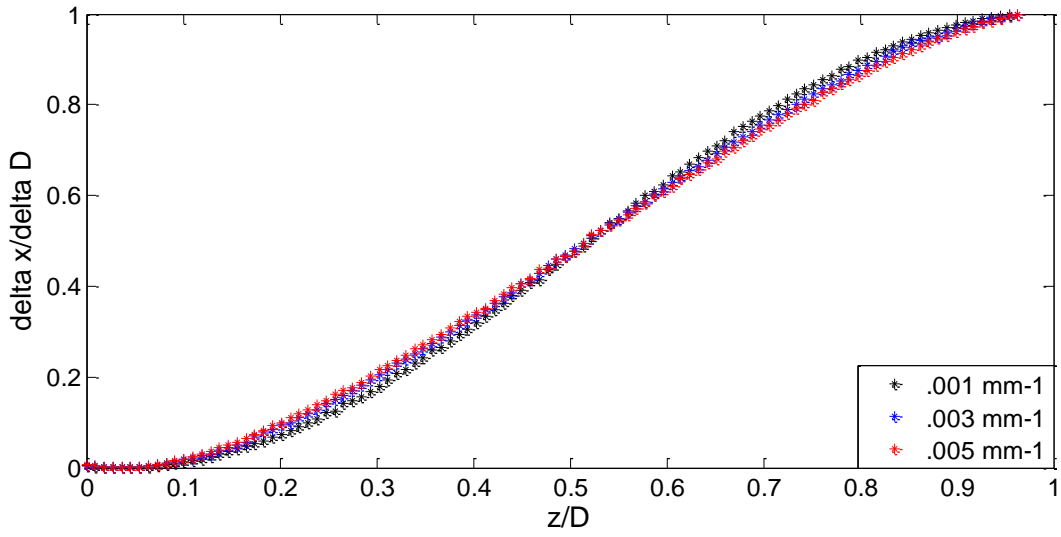
Sc = .72 mm-1
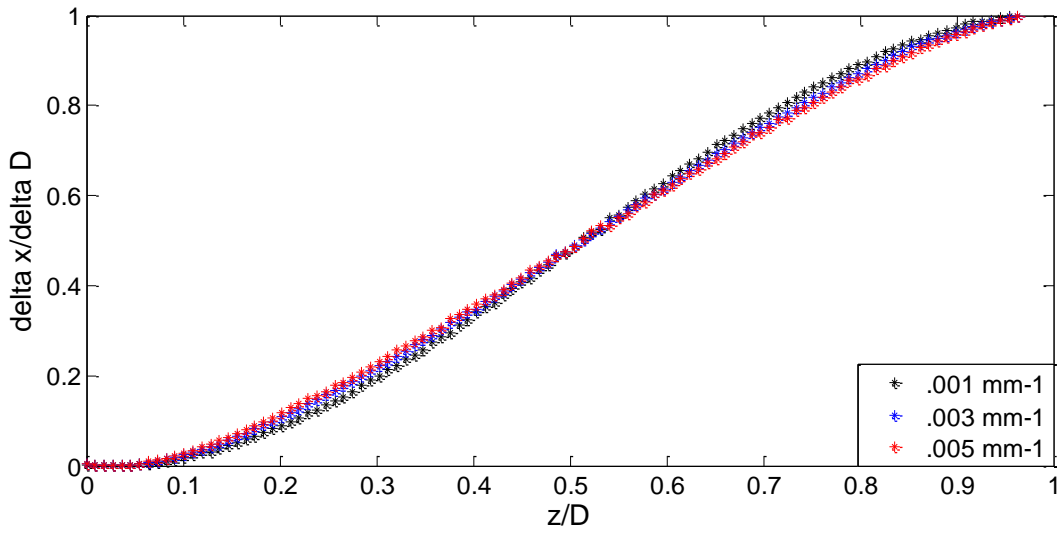
Sc = 1.0 mm-1
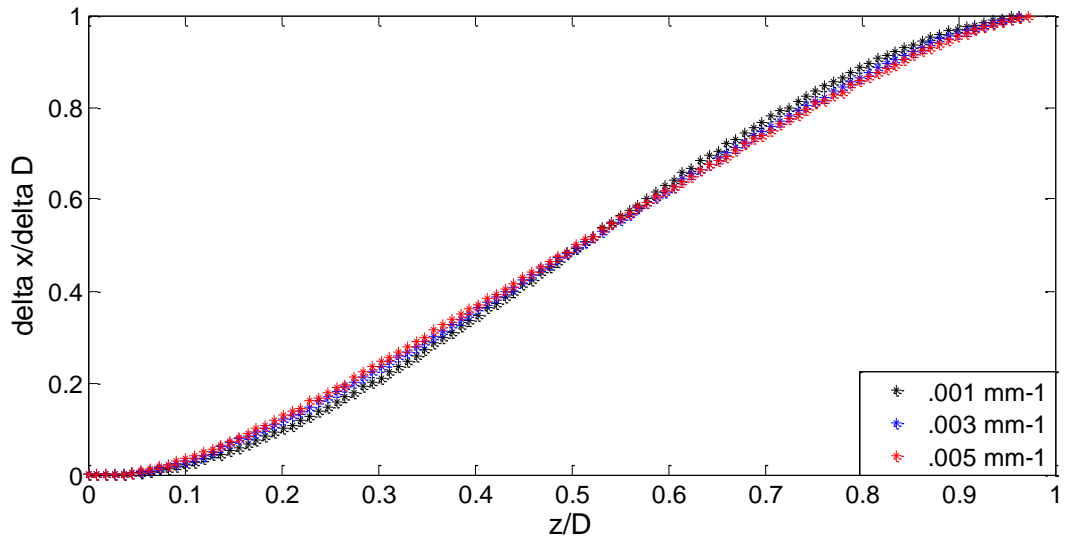
Sc = 1.5 mm-1
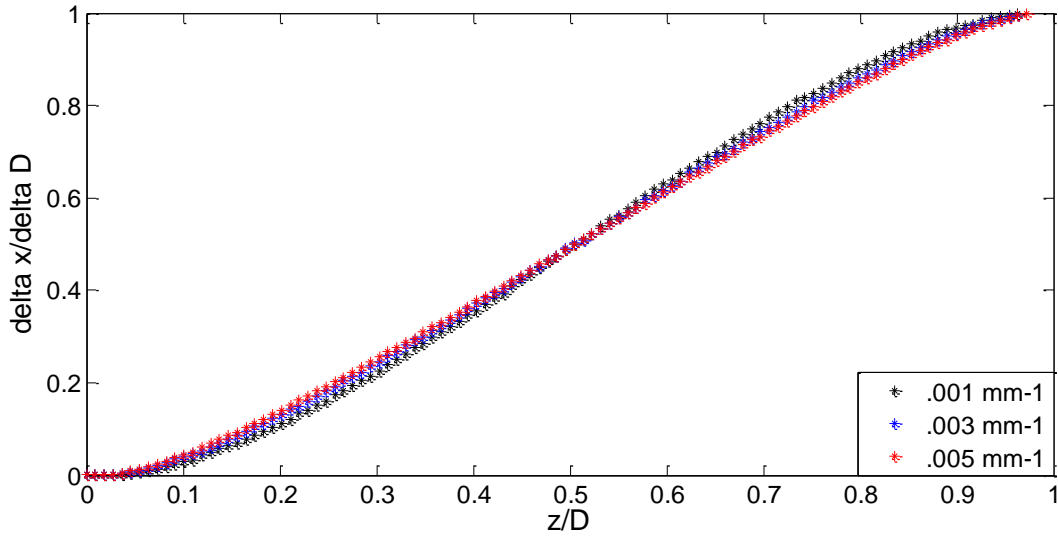
Error Graph for SC = .5, 1.5 mm-1, AC = .005 mm-1
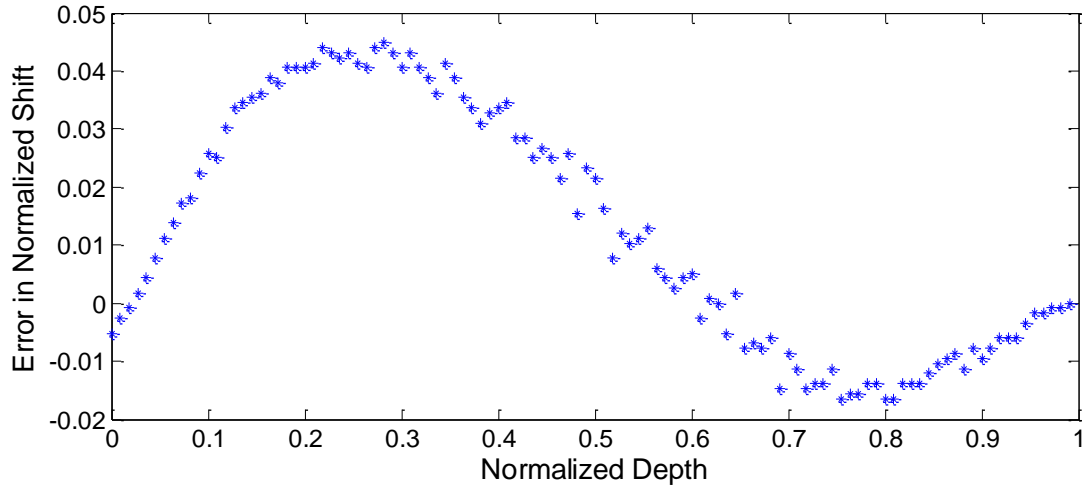
Error Graph for AC = .003, .005 mm-1, SC = 1.5 mm-1
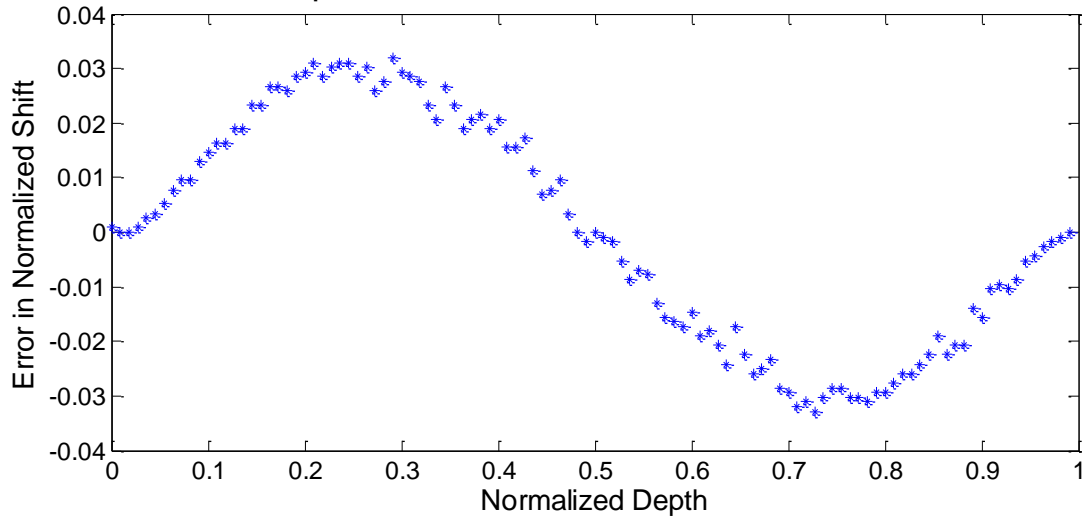
Figure 4.1. The first four figures are the calibration curves for varying μ'_s and μ_a. The first error graph shows the error curve between the extremes of μ_a with μ'_s kept constant at 1.5 mm^{-1}. Likewise, the second error graph shows the error curve between the extremes of μ'_s with μ_a kept constant at .005 m^{-1}.

4.1.2 Off-Axis Detector Distance

The reason why simulations with varying δD were performed for three cases of optical properties was to see if the sensitivity of the detectors to off-axis distance changed depending on their values. Visually it is apparent from Figure 4.2 that from the three cases, the case where μ_a and μ'_s are .005 and .5 mm^{-1} exhibit slightly more sensitivity to δD. As can be seen from the error graph, Overall, δD seems to not have a significant effect on the calibration curves. In fact, the maximum error experienced for the most sensitive case (μ_a = .005 mm^{-1}, μ'_s = .5 mm^{-1}) of .02 accounts for only .3 mm. Therefore, the difference in δD between the first and second source-detector configuration used for this study (Figure 2.2) does not cause a significant difference in the derived calibration curves.
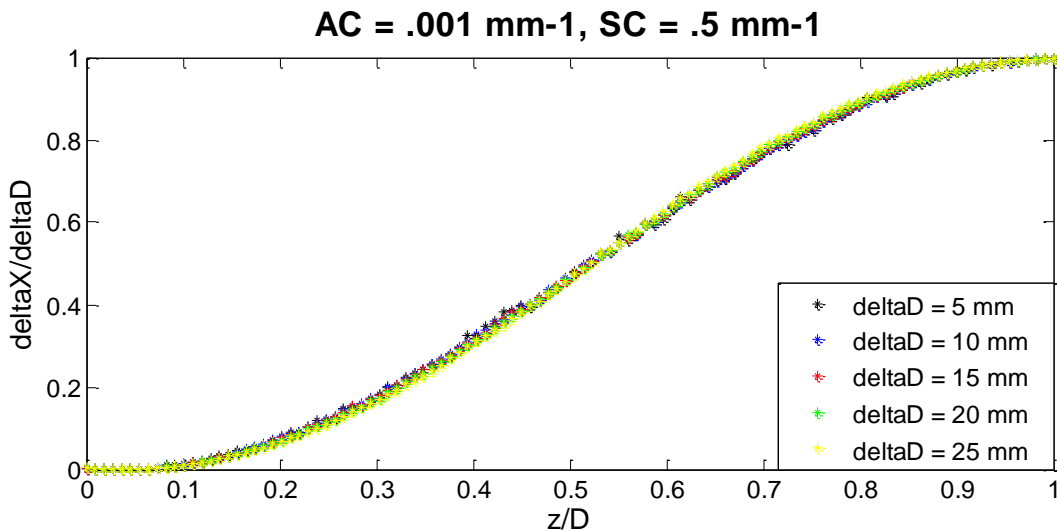
AC = .001 mm-1, SC = .5 mm-1
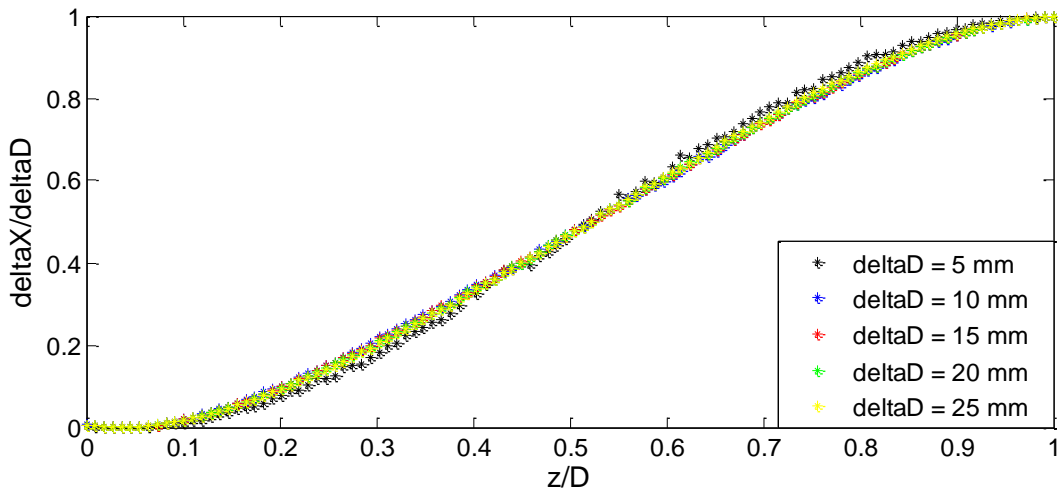
AC = .005 mm-1, SC = .5 mm-1

AC = .001 mm-1, SC = 1.5 mm-1
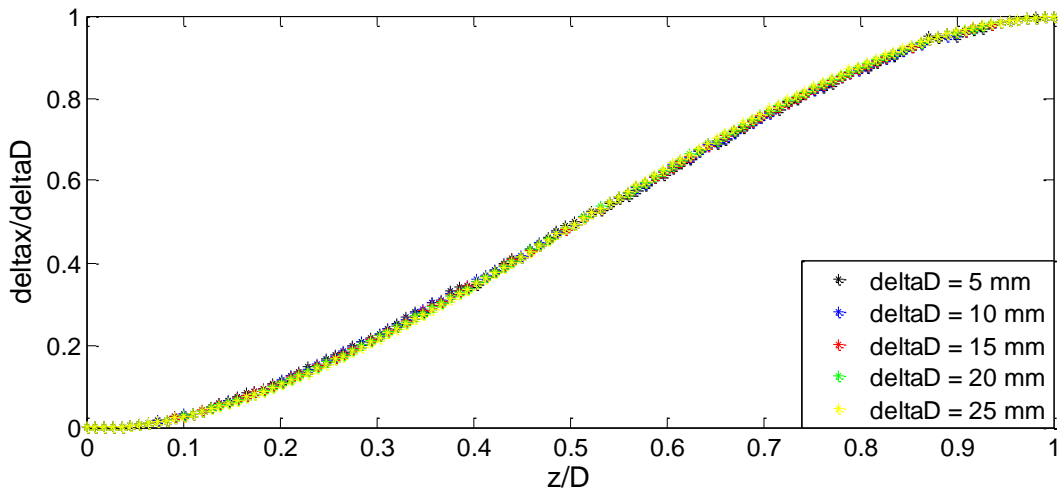
Error Graph for deltaD = 25 and 5 mm, AC = .001 mm-1, SC = .5 mm-1
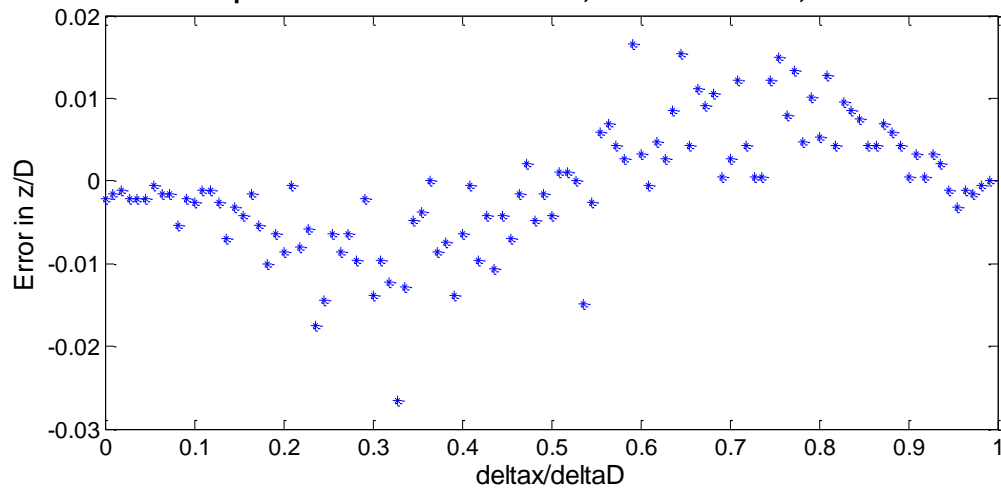
Figure 4.2. Calibration curves and error graph for different values of δD and different μ$_a$ and μ'$_s$. δD was varied from 5, 10, 15, 20, 25 mm and (μ$_a$, μ'$_s$) = (.001,.5),(.005,.5),(.005,1.5)(mm^{-1}).

As Figure 4.2 shows, the calibration curves experienced very little error between the four different cases of source position in the x-axis. The four cases considered four scenarios of source position along the x-axis in relation to the x-detector pair; (A) the source is to the negative side of both detectors, (B) the source is on top of the -x detector, (C) the source is between the -x detector and the midpoint between the detector pair, (D) the source is on the midpoint. Because the medium geometry was set to infinite, the law of symmetry can be applied for all four cases. Therefore, it can be concluded that as long as the source is on the axis of the detector pair, the calibration curves will experience negligible error.

Unlike Cases A through D, Cases D through I did experience error between the calibration curves (Figure 4.3). In particular, the error between shifts that translate to deeper depths (z/D ~ .6 to 1) appear to be the most affected with the normalized shift decreasing in that depth range as the source position increases in the y-direction. This could be due to the source being too far away for the emitted photons to reach the detector. In fact, as shown by case E and F, a discrepancy in the x-coordinate does not seem to affect the calibration curves.

AC = .001 mm-1, SC = 1.5 mm-1

Error Graph for Cases E through I
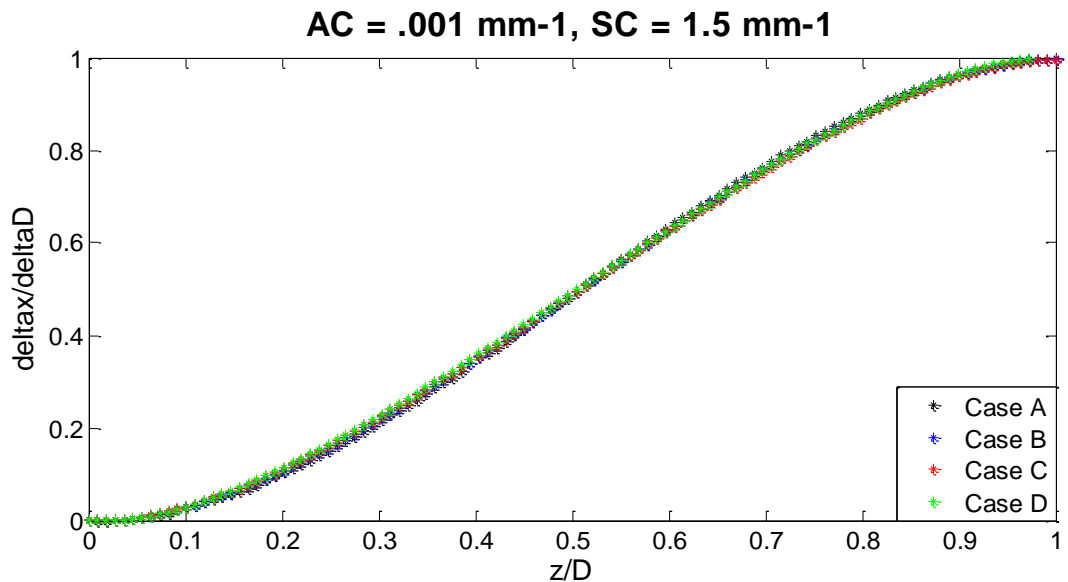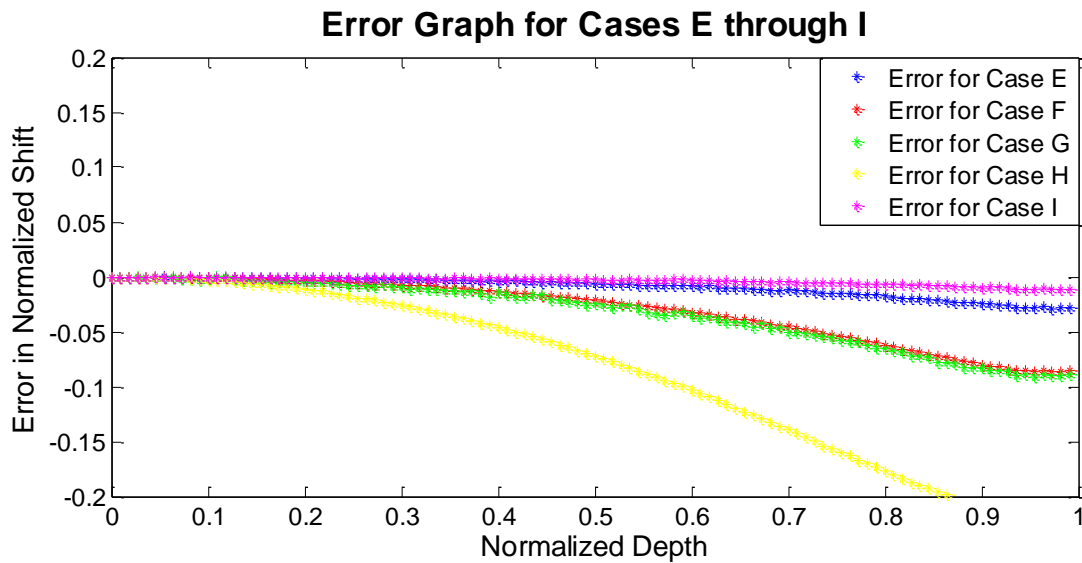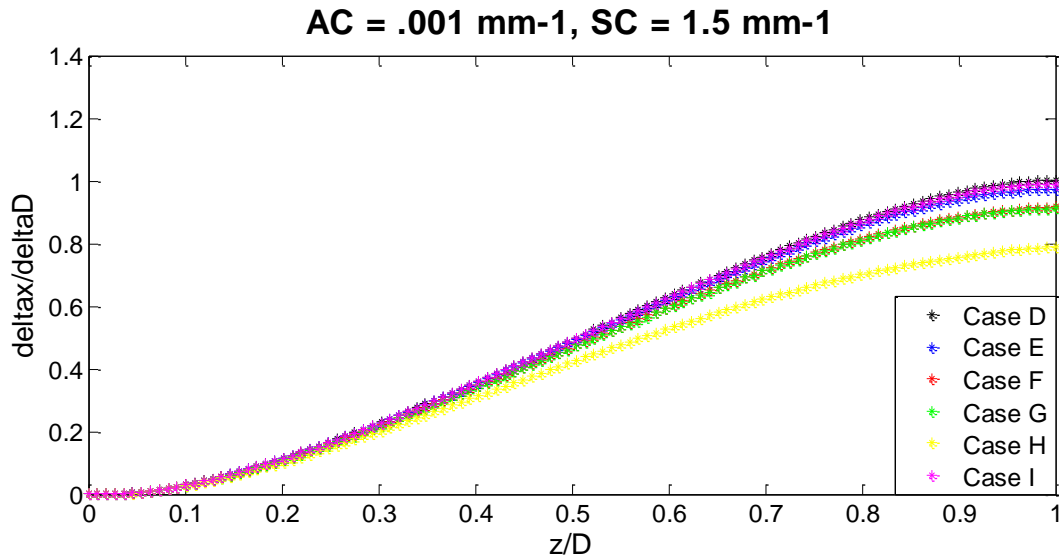
Figure 4.3 Calibration curves for the different cases of source position in relation to the off-axis x detectors presented in Section 3.1.3.

In a more general sense, from the response of the calibration curves to cases A through I we can make two conclusions about how accurately the source needs to be positioned in the x-y plane with relation to the detector pair in question. Firstly, there is a margin of at least ±24 mm

from the midpoint in the same axis of the detector pair in which the source can be positioned without affecting the calibration curves. Secondly, there is a margin of ~3 mm for the axis that is perpendicular to the axis of the detector pair. Although the first clause could possibly be increased to a higher range where the limiting factor has to do with the detectors being too far away to achieve sensitivity to the source, we will not experience errors that high during a typical experimental setup. The margin of ~3 mm in the perpendicular axis is sufficient enough for us to position the source by hand, as we typically get the source within a 2 mm radius of the midpoint. Thus, additional instrumentation/techniques were not required for source positioning.

4.1.3 Infinite vs. Slab Geometry

Figure 4.4.

Calibration curves and error graph for infinite and slab geometry. For both cases, μ_a = .001 mm^{-1} and μ'_s = 1.5 mm^{-1}.

Unlike the medium optical properties and δD, the change in geometry accounts for a more significant variation between calibration curves. It is apparent from Figure 2.8 that the off-axis shifts for the slab geometry case are generally less than that from the infinite geometry case for any depth. The maximum error of .13 accounts for a distance of 1.95 mm for a δD of 15 mm. This is approximately four pixels in the spline interpolated image. Interestingly, the majority of the error is experience for the middle depths, as opposed to the previous simulations which had most of the error in the deeper and shallower regions. Due to this discrepancy, we were careful to specify the geometry when performing simulations for a particular phantom.

4.2 Liquid Phantom Noise Characterization

It is apparent from the line graphs below that the intensity fluctuates as the source-detector traverses in the x-direction for each case. As expected, the addition of 30 ml of India Ink caused a significant reduction in the average photon count. The NSR was generally higher for high gain scans than low gain scans (Figure 4.9). However, because every NSR value from each scan was lower than .01, the differences between each case were deemed insignificant. Table 4.1 shows the NSR values for each case.

NSR				
	High Gain	High Gain w/Ink	Low Gain	Low Gain w/Ink
5.5 cm	.0040	.0091	.0049	.0181
7.5 cm	.0052	.0066	.0033	.0242
9.5 cm	.0061	.0101	.0054	.0115

11.5 cm	.0066	.0145	.0042	.0081

Table 4.1 Table of NSR values of each combination of gain, distance in the y-axis from back wall, and addition of 30 ml of India Ink.

Interestingly, there was no noticeable trend between position of the source-detector configuration in the x-y plane and optical intensity values. It was expected that the boundaries, especially those adjacent of the back wall, front wall, and liquid surface, would cause a distinct photon intensity loss due to absorbed or escaped photons. This means the image space that is traversed for the scans performed in this study should effectively be considered an infinite medium geometry in the basis that the boundaries are not affected by their proximity to the PVC walls of the tank. Therefore, we confirmed that setting the medium geometry to infinite in the D&P software should be an adequate enough of a characterization of the liquid phantom medium. This also tells us that any error between the calculated and actual depths of the rods have a lesser likelihood of being due to the geometry not being accurately described in the D&P software.
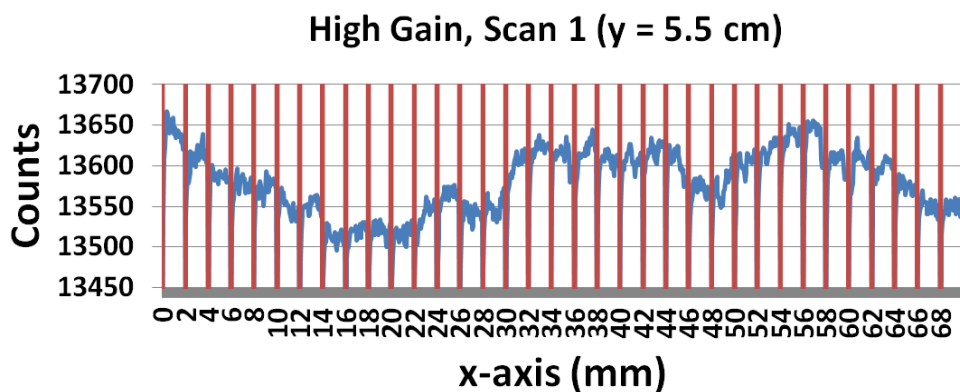
High Gain, Scan 2 (y = 7.5 cm)

x-axis (mm)
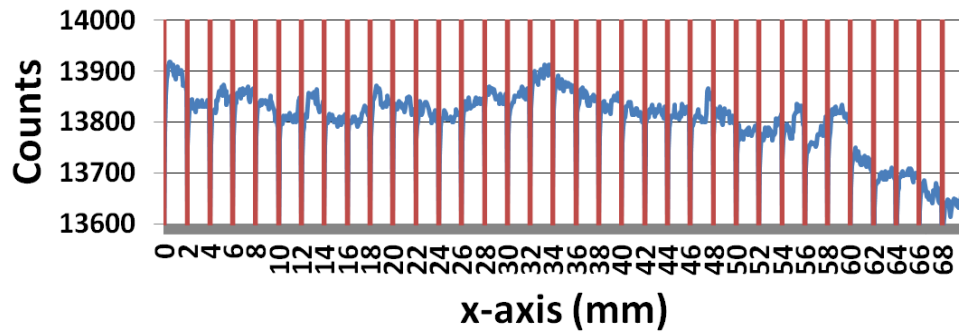
High Gain, Scan 3 (y = 9.5 cm)

x-axis (mm)
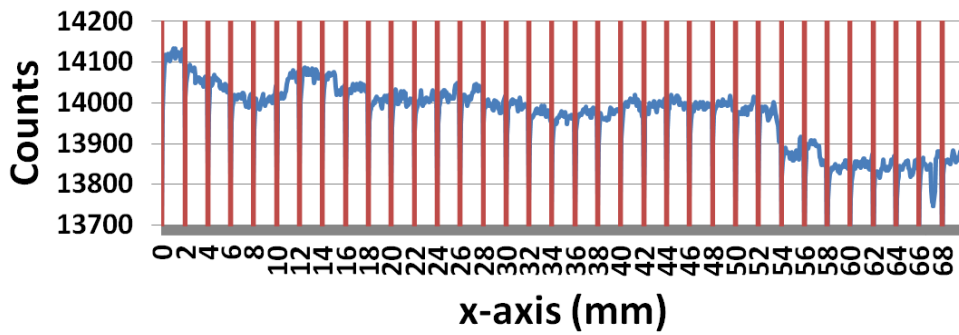
High Gain, Scan 4 (y = 11.5 cm)
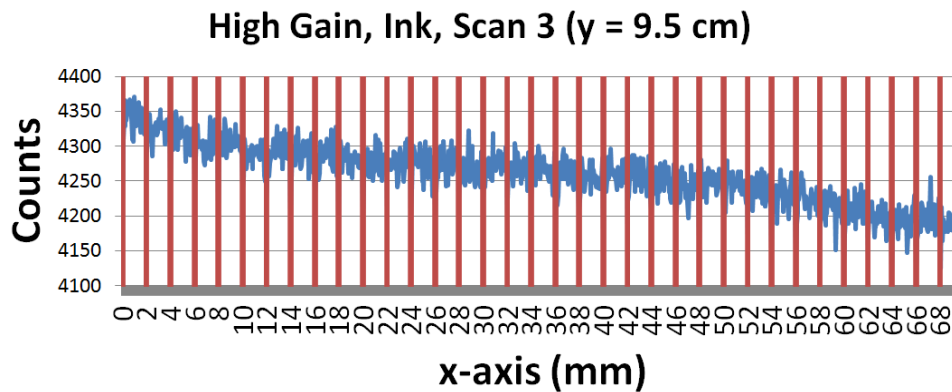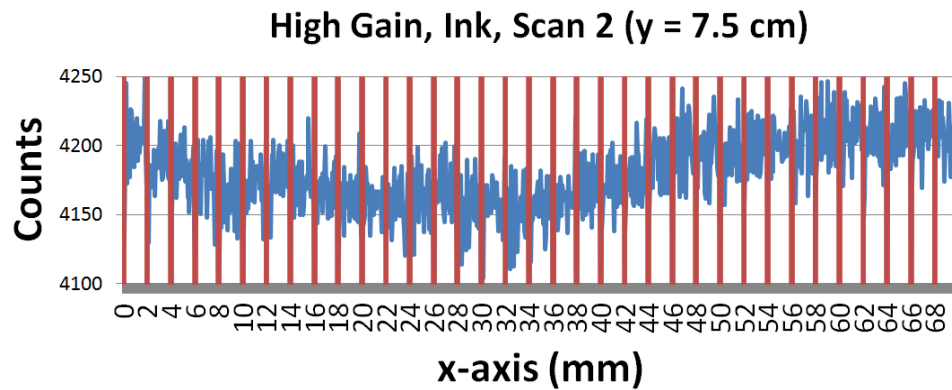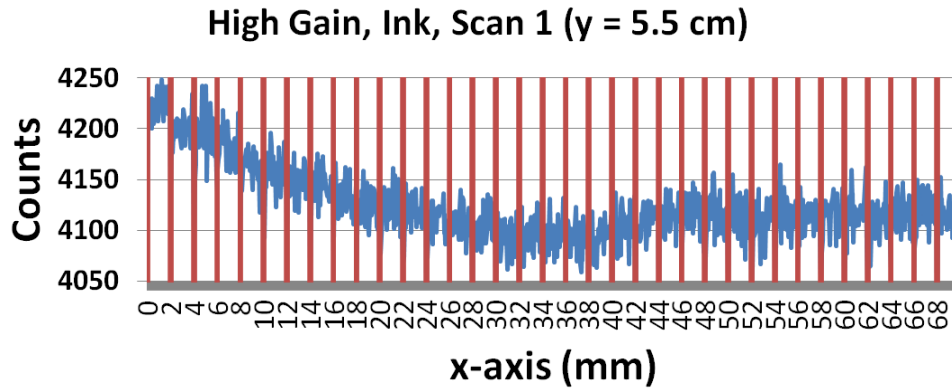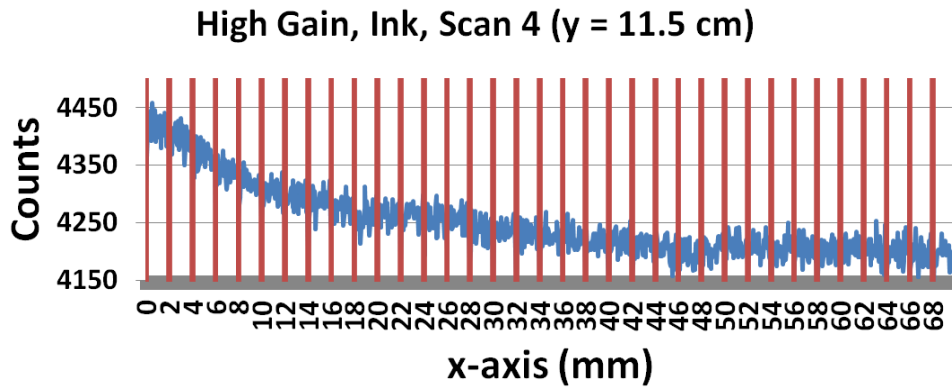
x-axis (mm)
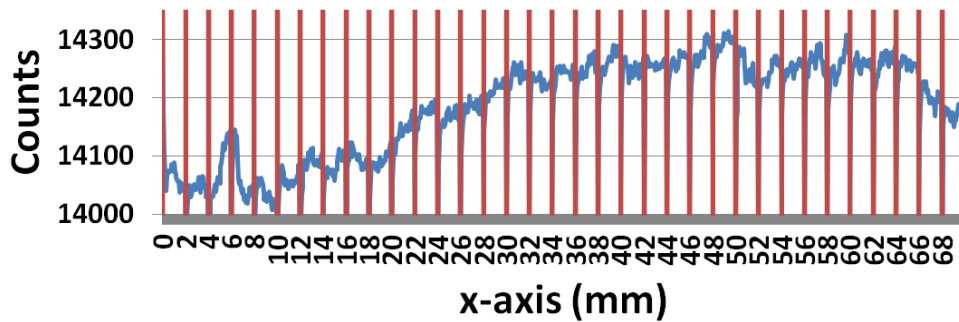
Figure 4.5 Noise scans performed with high gain and 30 ml of India Ink added to the mixture.
Shown in the top right of each graph is the NSR. The red vertical lines mark the first point for
each sampling location in the x-axis.

High Gain, Ink, Scan 1 (y = 5.5 cm)

High Gain, Ink, Scan 2 (y = 7.5 cm)

High Gain, Ink, Scan 3 (y = 9.5 cm)

High Gain, Ink, Scan 4 (y = 11.5 cm)

Figure 4.6 Noise scans performed with high gain and 30 ml of India Ink added to the mixture.

Low Gain, Scan 1 (y = 5.5 cm)

Low Gain, Scan 2 (y = 7.5 cm)

Low Gain, Scan 3 (y = 9.5 cm)

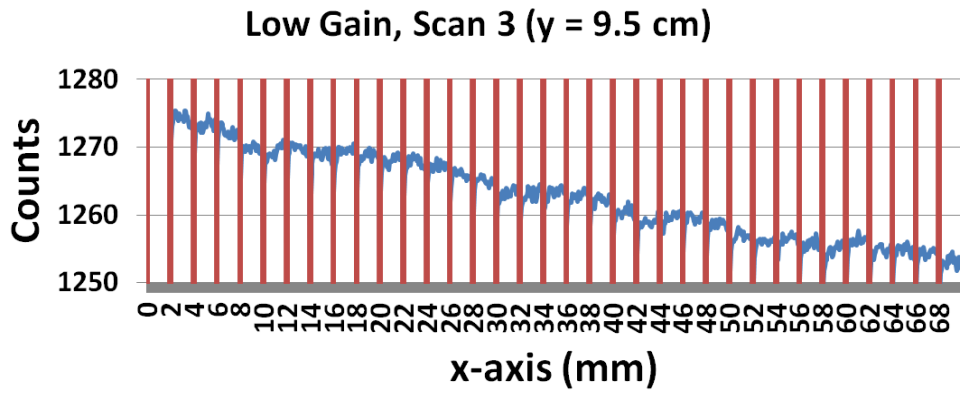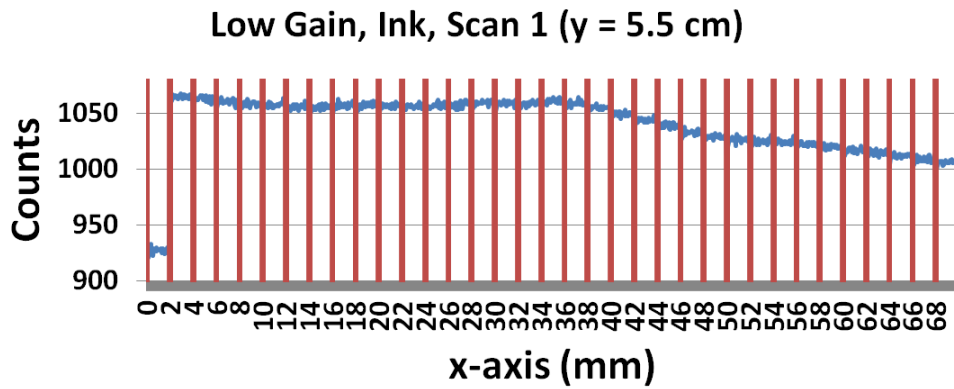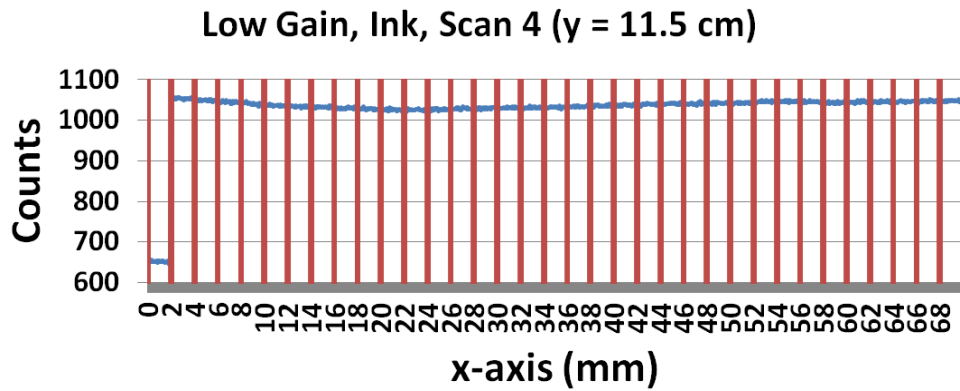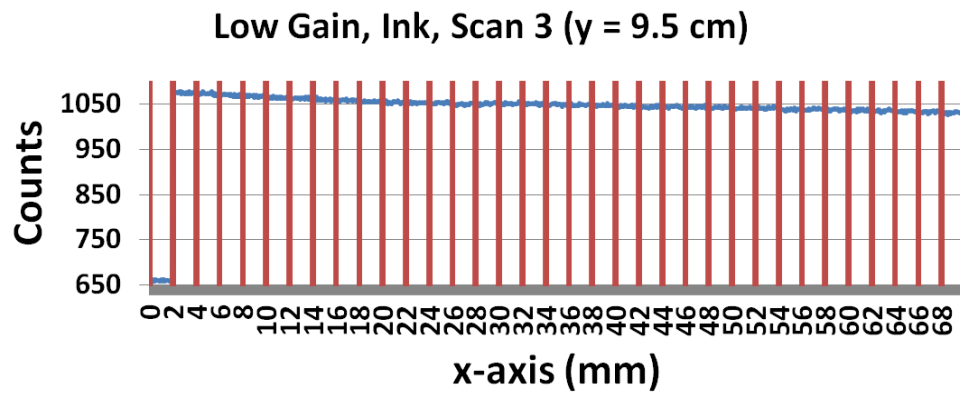**Low Gain, Scan 4 (y = 11.5 cm)**
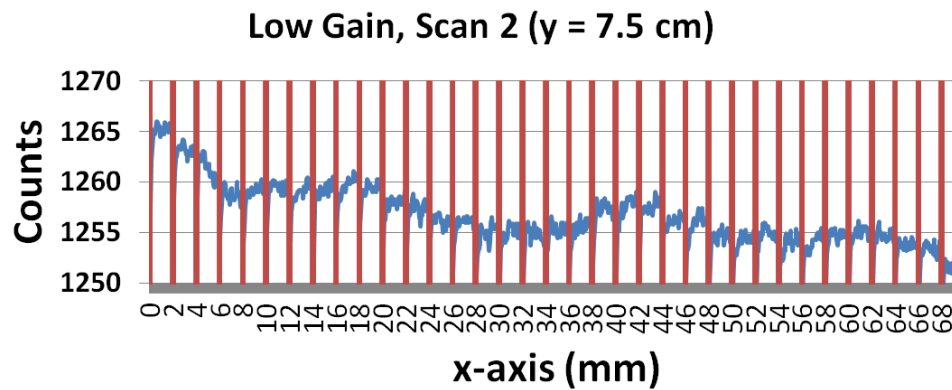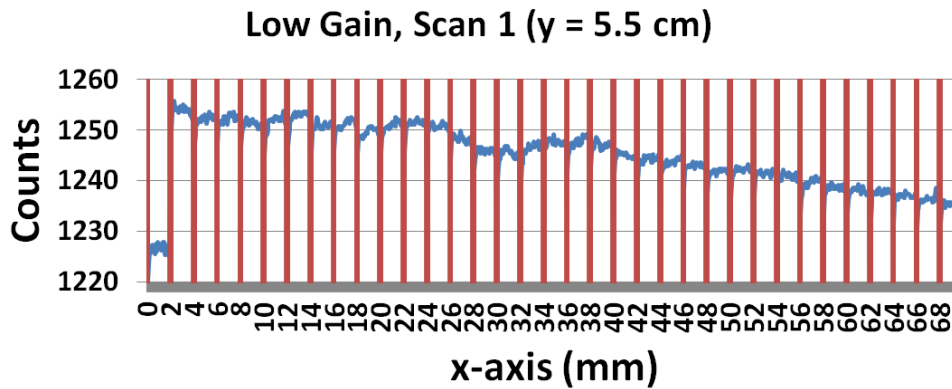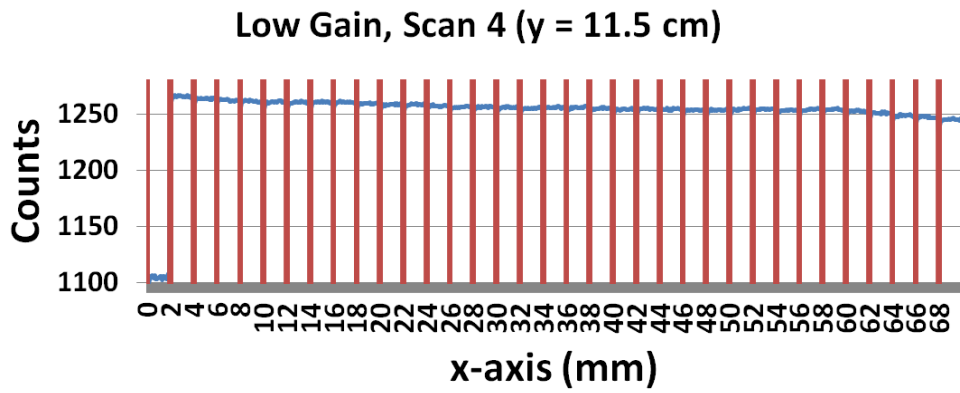
Figure 4.7 Noise scans performed with low gain and without India Ink added to the mixture.

Low Gain, Ink, Scan 1 (y = 5.5 cm)

Low Gain, Ink, Scan 2 (y = 7.5 cm)

Counts vs x-axis (mm)

y-axis: 800, 900, 1000, 1100

x-axis (mm): 0, 2, 4, 6, 8, 10, 12, 14, 16, 18, 20, 22, 24, 26, 28, 30, 32, 34, 36, 38, 40, 42, 44, 46, 48, 50, 52, 54, 56, 58, 60, 62, 64, 66, 68

Low Gain, Ink, Scan 3 (y = 9.5 cm)

Counts vs x-axis (mm)

y-axis: 650, 750, 850, 950, 1050

x-axis (mm): 0, 2, 4, 6, 8, 10, 12, 14, 16, 18, 20, 22, 24, 26, 28, 30, 32, 34, 36, 38, 40, 42, 44, 46, 48, 50, 52, 54, 56, 58, 60, 62, 64, 66, 68

Low Gain, Ink, Scan 4 (y = 11.5 cm)

Counts vs x-axis (mm)

y-axis: 600, 700, 800, 900, 1000, 1100

x-axis (mm): 0, 2, 4, 6, 8, 10, 12, 14, 16, 18, 20, 22, 24, 26, 28, 30, 32, 34, 36, 38, 40, 42, 44, 46, 48, 50, 52, 54, 56, 58, 60, 62, 64, 66, 68
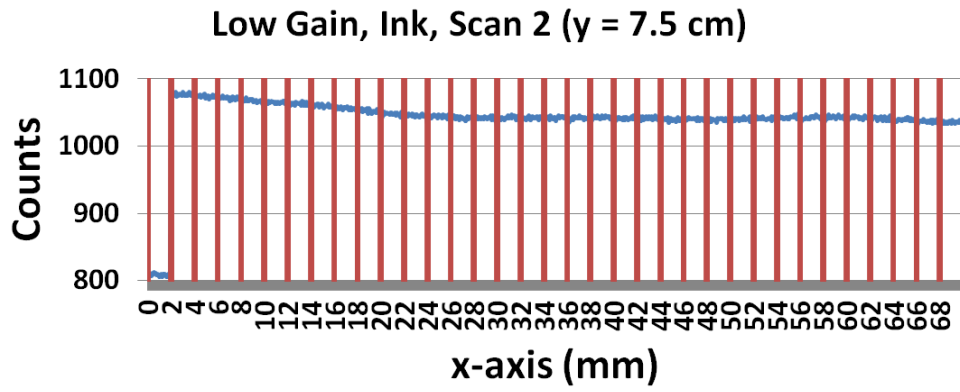
Figure 4.8 Noise scans performed with low gain and 30 ml of India Ink added to the mixture.
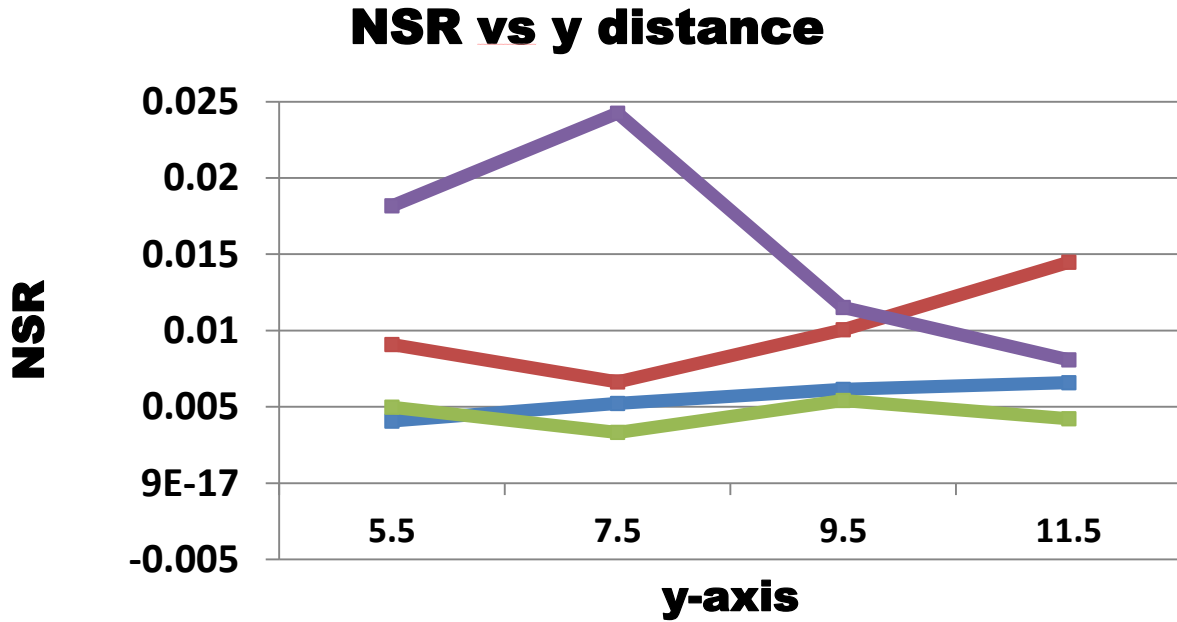

Figure 4.9 Error graph between the NSR for the four different line scans. Blue - High Gain, Maroon - High Gain w/Ink, Green - Low Gain, Purple - Low Gain w/Ink.

4.3 Depth Discrimination Results

4.3.1 Case I

Figure 4.10 shows the depth results as a function of the y direction for the different 6 different depths chosen for this case. We only used the x-detector pair for these experiments as the maximum gradient direction of the rods were parallel to the x-axis. For some depths, the calculated depth was not consistent throughout the y-direction. This was not considered to be a critical as the maximum error was caused by a discrepancy of 1 pixel (.5 mm) in the off-axis shift calculation. It should also be noted that the calibration curve used to solve for the depths of the rods for this experiment were derived using a μ_a and μ'_s of .001 and 1.5 mm^{-1}, respectively for a source-detector separation distance (D) of 65 mm.

From Figure 4.10, it is obvious that the shallower depths (z = 10 mm, 20 mm) experience the most error. However, contrary to our expectations, the calculated depths seem to get more accurate the deeper the rod was located (Figure 4.11). For instance, the rod at z = 10 mm and z = 55 mm are both ~15% of the separation distance (65 mm) from the source and detector, respectively. Unlike the depth calculation for the rod at 55 mm which comes within 1 mm of the actual depth, the depth calculation for the rod at 10 mm overestimates the depth by ~8 mm. As earlier, our margin of error is the width of a rod which is ~5 mm. After further inspection of the calibration curve, it was apparent that the calibration curves were not symmetric, thus causing the asymmetry in the depth calculations. In fact, it was found that the linear portion of the calibration curve expanded a range of normalized depths (~.35 - .85) that included deeper regions. Therefore, with this new range for the linear portion of the calibration curve it makes sense that z = 10 mm (z/D =.15), 20 mm (.30) experience the most error. Likewise, it also makes sense that the deeper depths, z = 50 mm (.77), 55 mm (.84), will experience the less error.
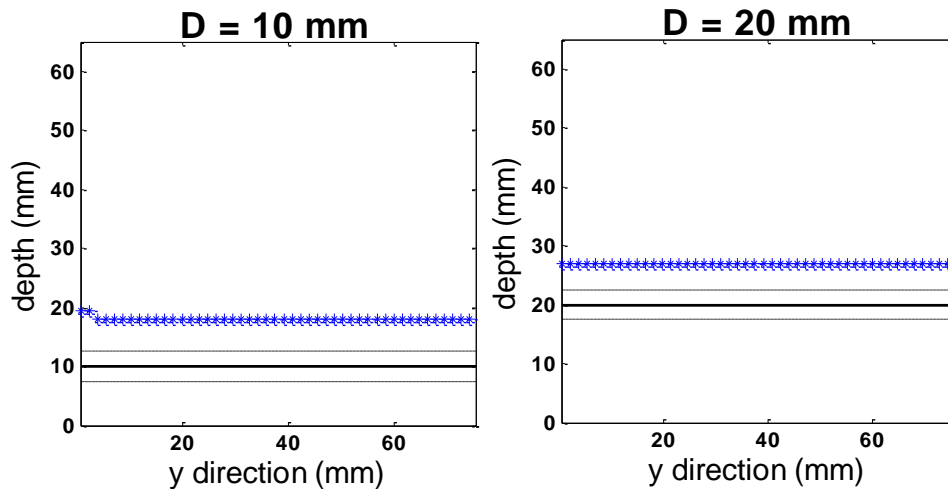
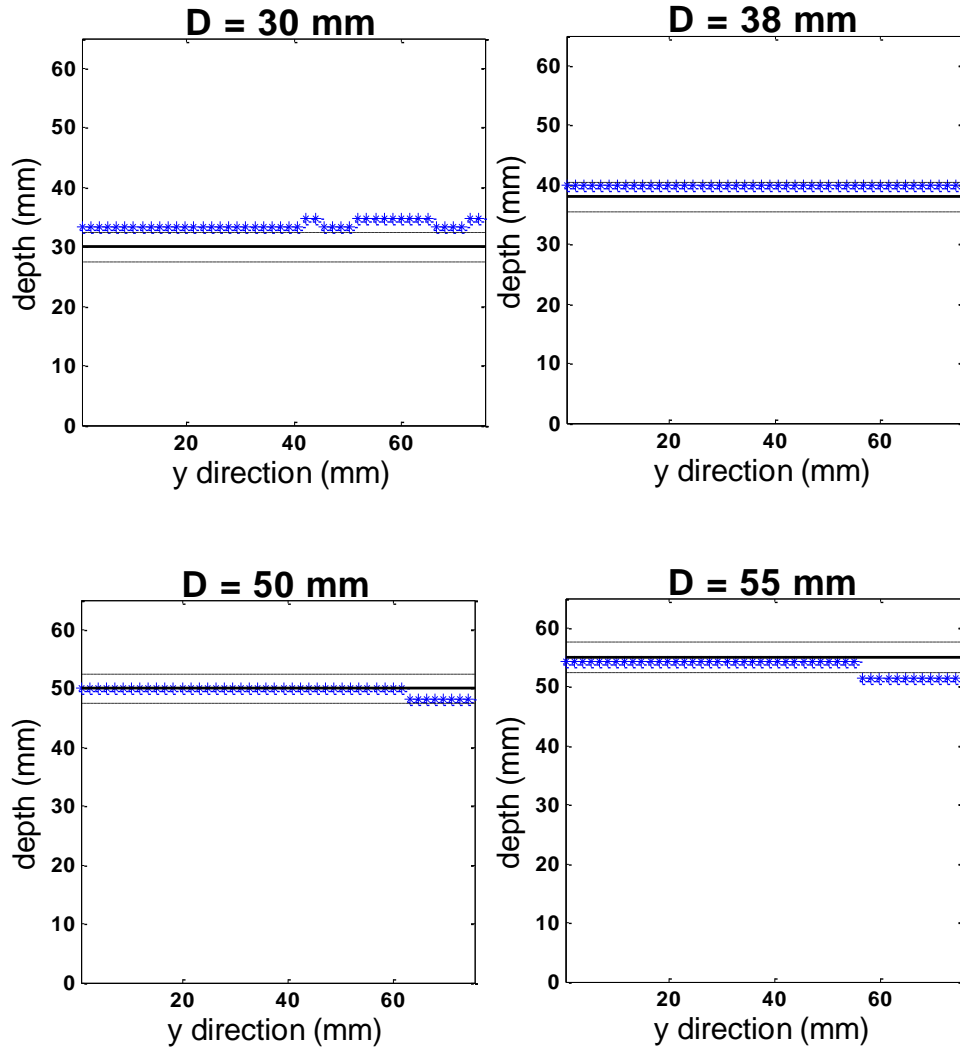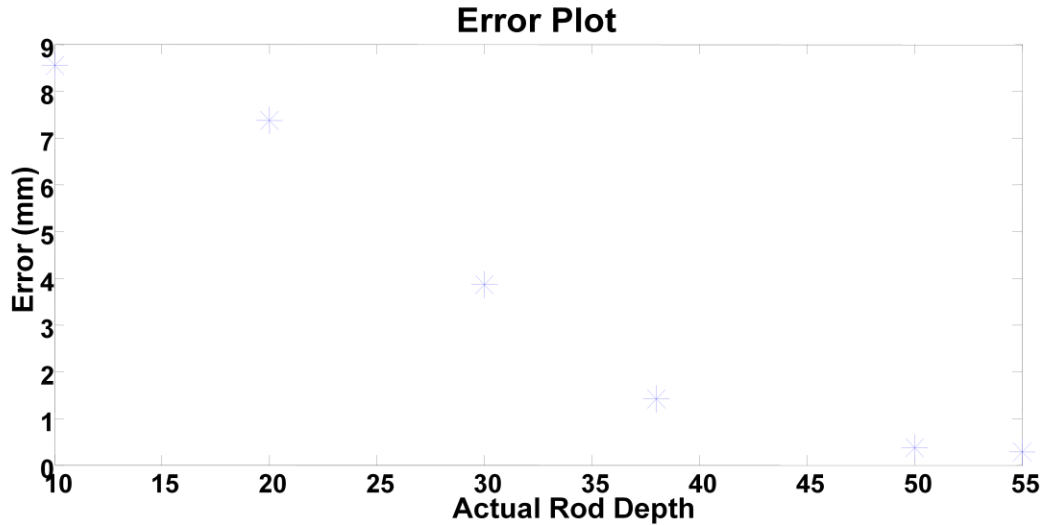*Figure 4.10 Results of Case I.*

Figure 4.11 Error plot between calculated and actual rod depth for Case I.

4.3.2 Case II

The main objective of the experiments of Case II were to investigate how the angle of the rods in the x-y plane affected the depth calculation and error of the rod. As mentioned in Section 3.3.4, the depth of the rod for every angle used in this experiment was $32.8 \pm .5$ mm.

Figure 4.12 shows one particular row from each detector image and the off-axis shift between each detector pair. The first time we ran the scans for this case, the source-detector cofiguration was programmed to traverse the x-direction for both the x-detector pair and y-detector pair scans. Looking at Figure 4.12, it is apparent that the y-detector pair scans suffered from noise fluctuations, and therefore it was difficult to calculate the off-axis shift between the y-detectors for some angles. This difficulty in calculating the off-axis shift between the y-detectors manifested in the sporadic error in the y-detector depth results shown in Figure 1.3 (top two graphs). To account for the detector pair direction, the experiment was repeated with the source-detector configuration traversing in the y-direction for the y-detector pair.
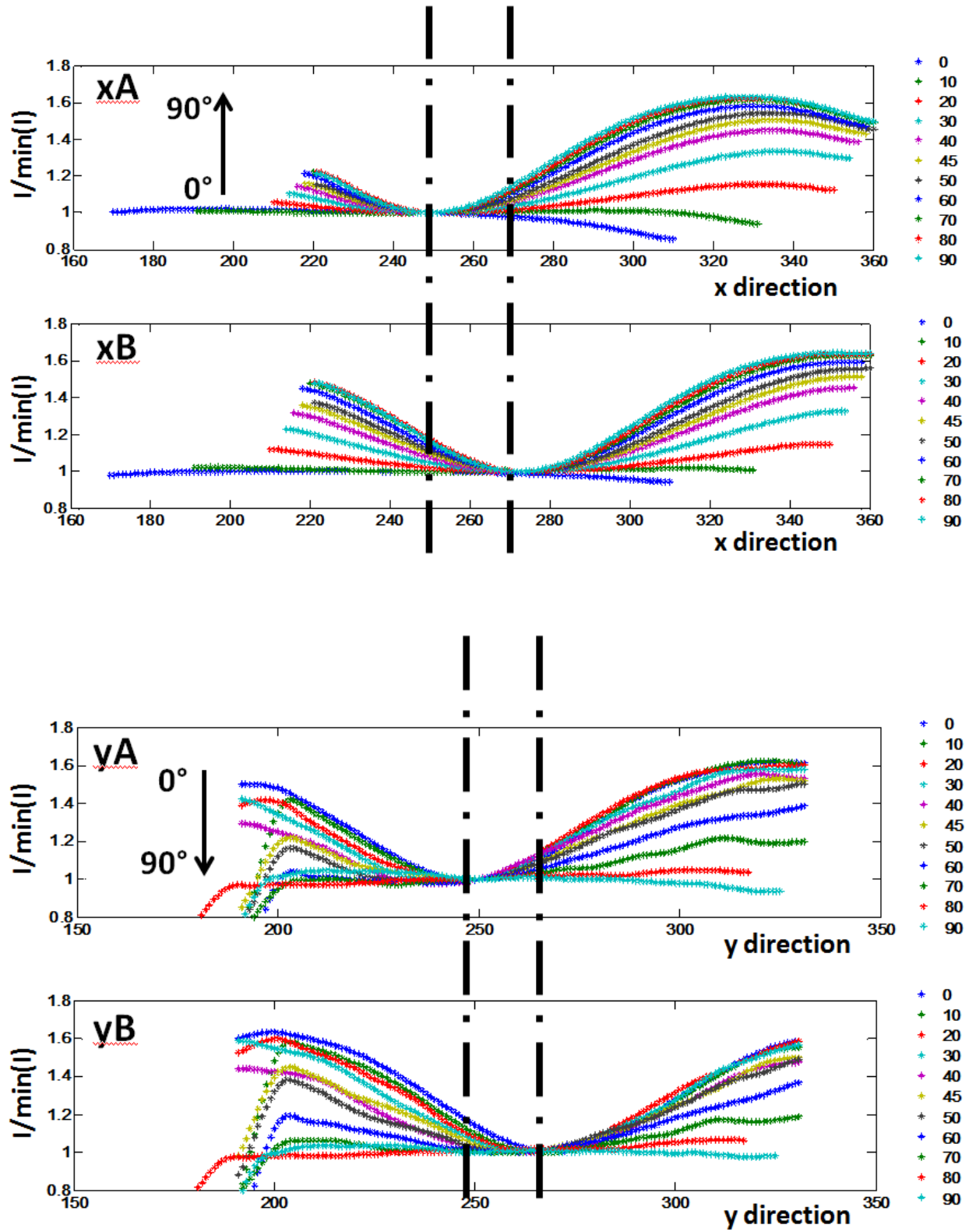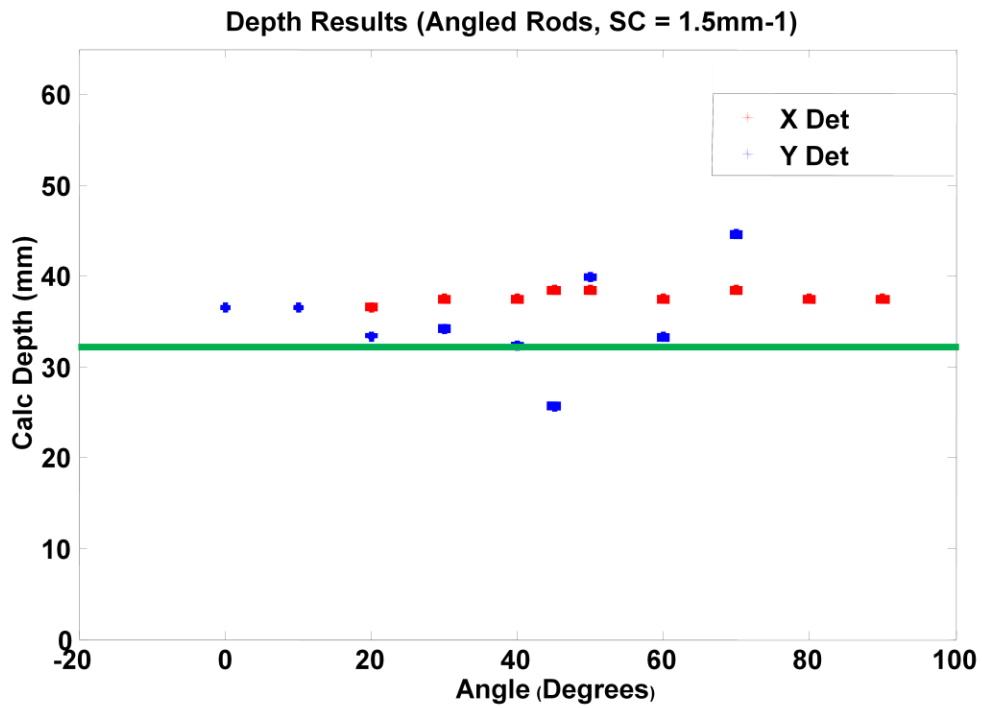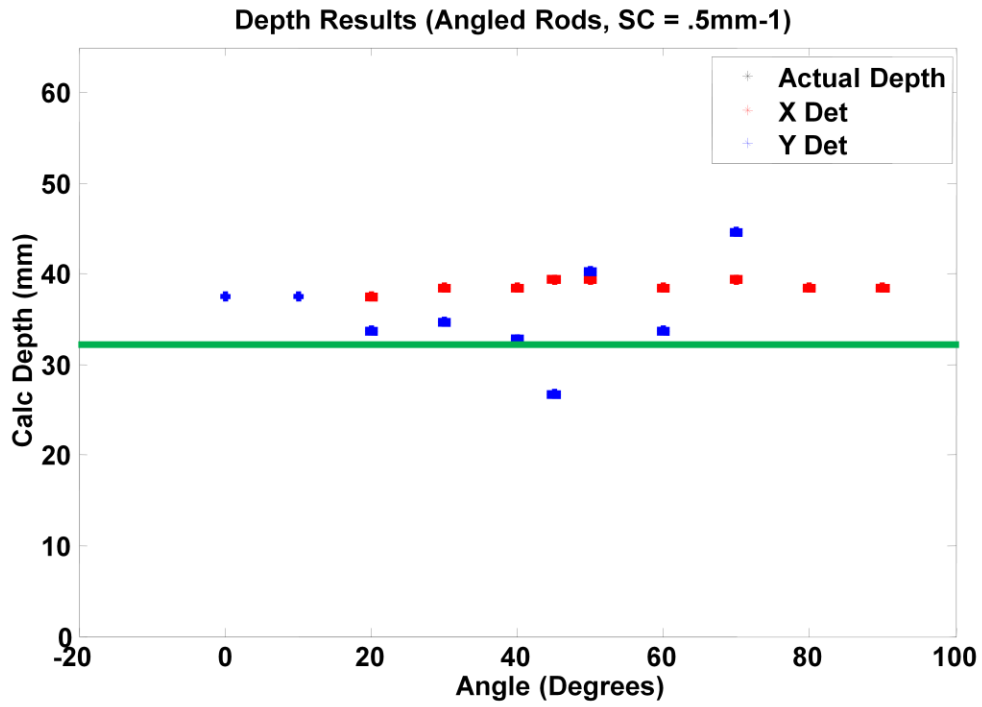
Figure 4.12 One particular line scan for Case II for both the x and y detector pairs.

Depth Results (Angled Rods, SC = .5mm-1)

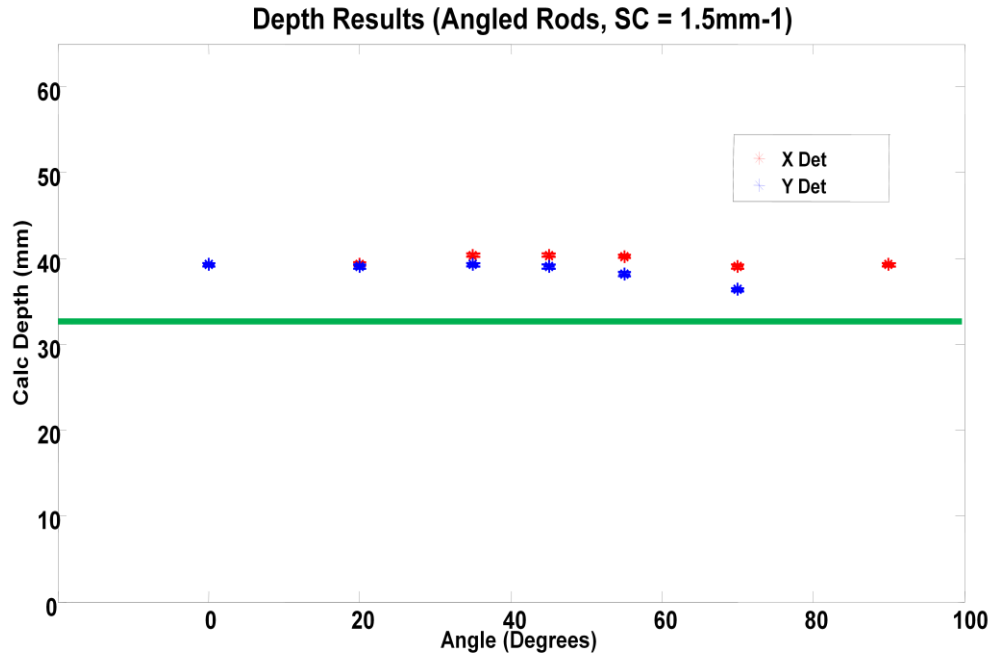**Depth Results (Angled Rods, SC = 1.5mm-1)**

Figure 4.13 Depth results for the different angles of Case II. The 1st and 2nd graphs were when the μ'$_s$ used to derive calibration curve was at .5 and 1.5, respectively. The 3rd graph were the results after the correction to the scan direction for the y-detector pair.

The peaks caused by the rod become increasingly broader and shallower for the x-detectors as the angle gets closer to 0°. This is expected because as the angle gets smaller, the line that connects the two x-detectors passes through a larger cross-distance of the rod. Eventually, when the rod is parallel to the x-axis, the peaks become less and less visible due to the decreasing sensitivity of the x-detector pair to the rod. The opposite is true for the y-detector pairs. Interestingly, for the angles in which the x-detector pair and y-detector pair were sensitive enough to the rod that a depth could be calculated, there was no visible trend between increasing angle size and depth error. Instead, there was a consistent systematic error of approximately +8 mm. This is in contrast to the error of ~ +2 mm for the rod at z = 30 mm from Case 1.

4.3.3 Case III

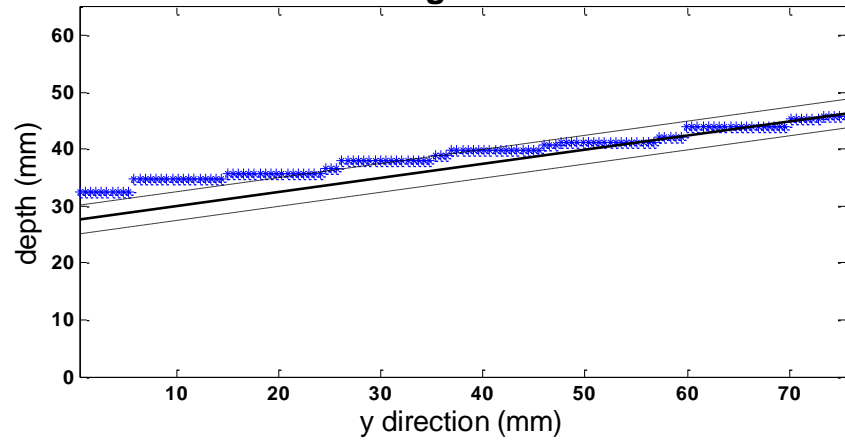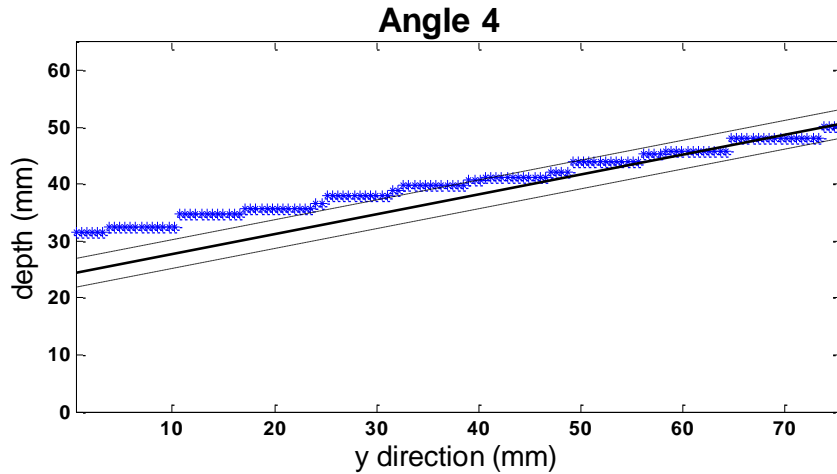## Angle 1
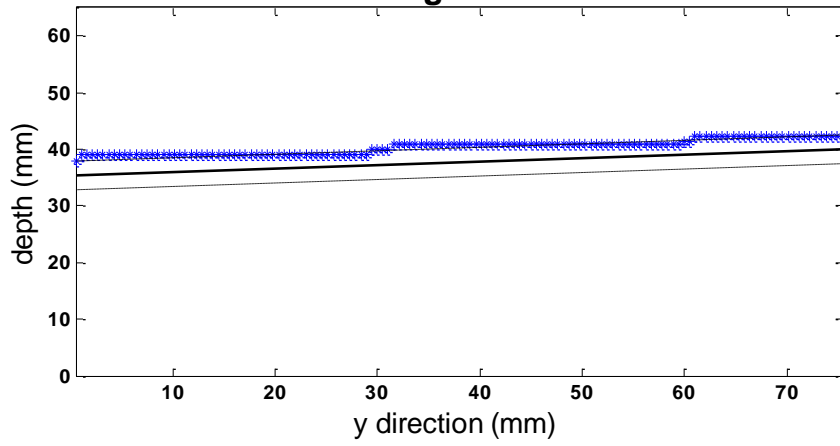
Angle 2
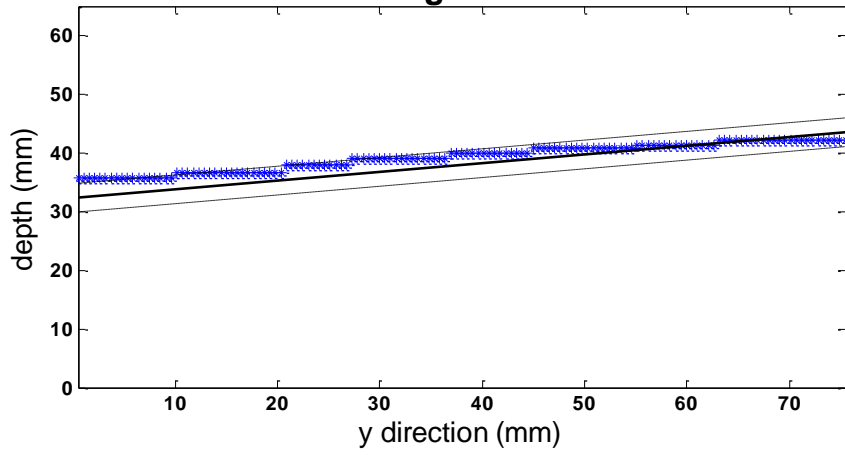
Angle 3

*Figure 4.14 Depth vs. y-axis for the four angles used in Case III.*

Figure 4.14 shows the results of Case III, in which the rods were parallel to the y-axis and angled along the depth direction. The results are consistent with the results from Case I, as the error between the calculated and actual depth decrease as the rod gets deeper in the y direction. What is also apparent from these graphs is how the spatial resolution in the x-direction limits the resolution in the depth direction. For instance, the graph for Angle 1 (the smallest angle) shows a total of three different calculated depth values throughout the length of the rod that was imaged. This lack of precision is caused by the fact that the off-axis shift is measure by pixels of finite size. Thus, for the spatial sampling rate of 2 mm^{-1}, the off-axis shift can be calculated within .5 mm of the actual value. The ideal case in which the every point of the rod along the y-direction will have a unique calculated depth would require infinitely small pixels. However, even for this ideal case, discretization will still exist in the depth direction as the calibration curve itself is also discrete.

4.3.4 Case IV

The experiments of Case IV involved overlapping rods in the depths and arrangements shown in Figure 3.8. As mentioned in Section 3.3.6, the purpose of this experiment was to attain

a qualitative understanding of the response of the depth discrimination algorithm to areas in which the rods intersect in the x-y plane. It should be noted that all the rods used in these experiments were at a constant depth.

The first scan involved a rod (Rod 1) parallel to the y-axis, as well as a rod (Rod 2) angled in the x-y plane. Figure 4.15 shows the 2nd derivative image as well as the line graph for row 15 for the three different 2nd rod angles. We picked row 15 as this was one of the few rows in all three images where both peaks are visible for each rod. Mainly, it demonstrates that for local areas around the intersection of the rods, it becomes difficult to distinguish the peak of the Rod 2 as it becomes engulfed by the larger peak of Rod 1. This was expected as the direction of the x-detector pair is perpendicular to Rod 1 and therefore is more sensitive to Rod 1 than Rod 2. It is also apparent that in the local intensity where both rods intersect have lower relative intensity than areas where there is only one rod. This was also expected as the fact that in the areas where the rods intersect, they both work to attenuate the detected optical signal through absorption.
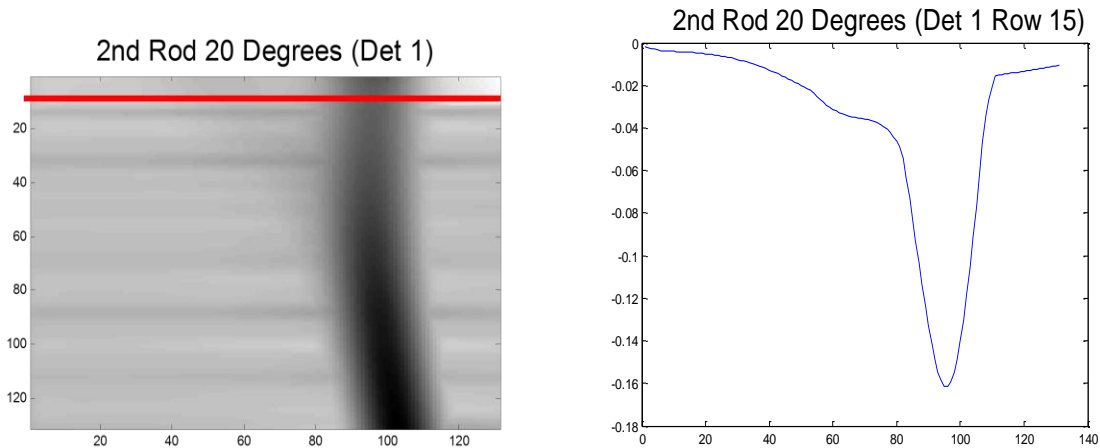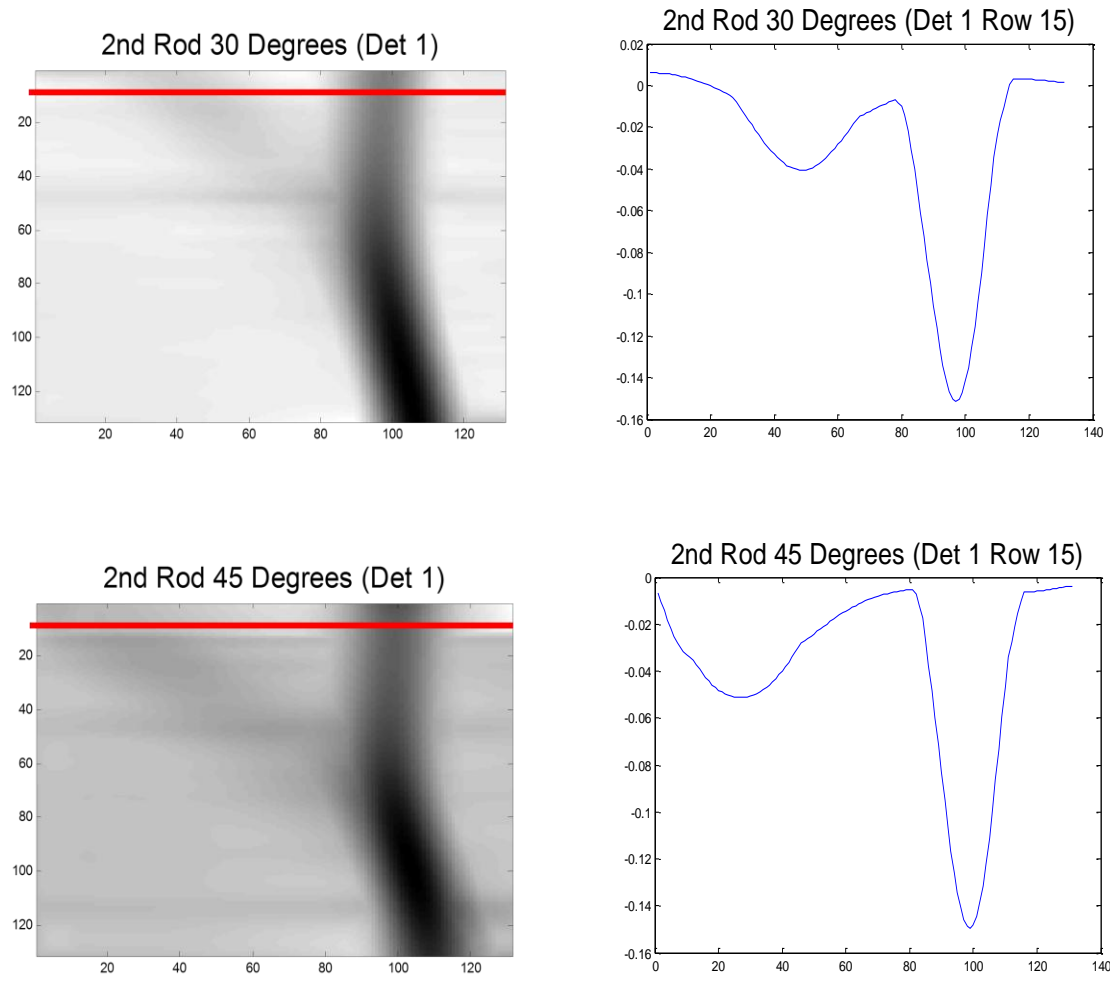
Figure 4.15 (left column) 2nd derivative images for the three different angles for the angled rod. (right column) Their respective line graphs for the 15 row of each graph (red line).

The error for both rods increase for areas that are proximal to the intersection. This can be seen in Figure 4.15. There are sevaral possible reasons for this discrepancy. For one, as the rods get closer in the x-y plane, the spatial location of the peaks for one or both of the rods may change due to merging of the two peaks. Another possibility is that the broadening of the angled rod's peak closer to the intersection may cause an increased incidence of error when calculating the peak position in Matlab. As Figure 4.16 shows, the scan for the case in which both rods were angled experienced similar depth error characteristics as well.

One deficiency from both scans was that the image space that was scanned was not big enough to capture both sides of the intersection. Also, there were numerous rows where the depth of the rods could not be calculated because the peaks had been merged. A bigger image space where the intersection of the rods reside in the center may be more informative in terms of investigating any symmetry in depth calculations between both sides of the intersection.

2 Angled Rods Depth Graph
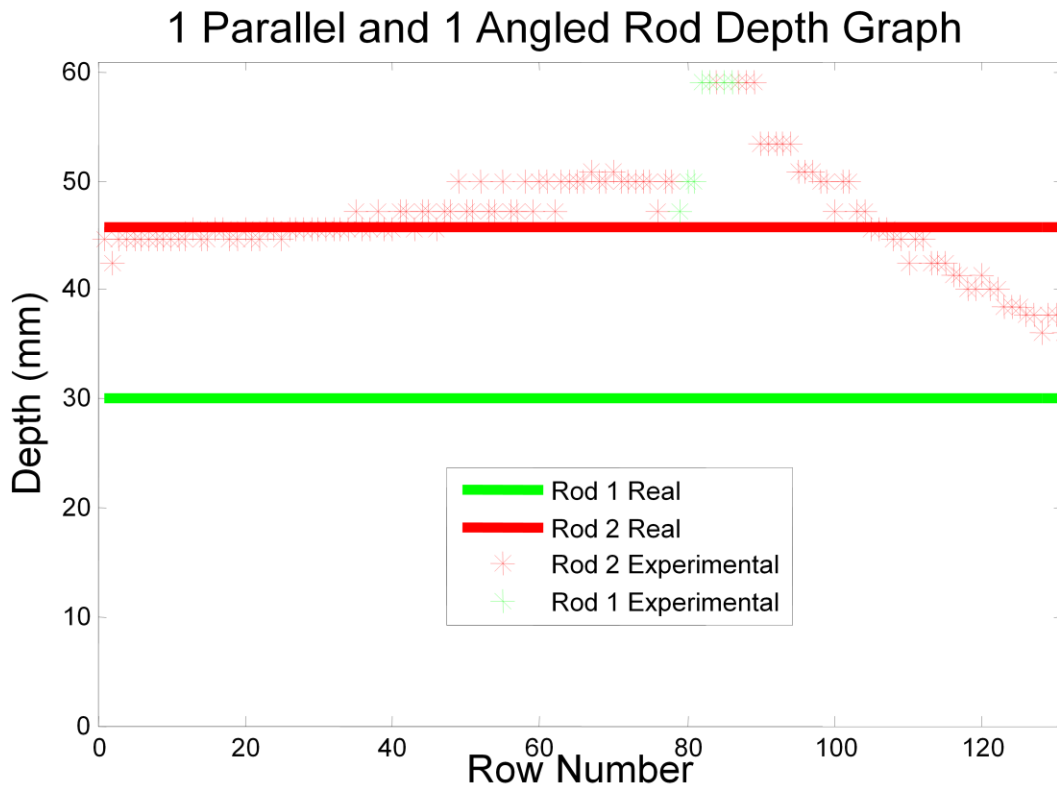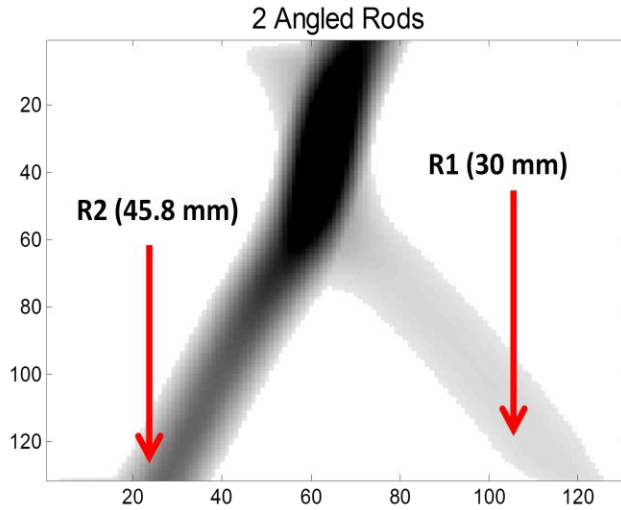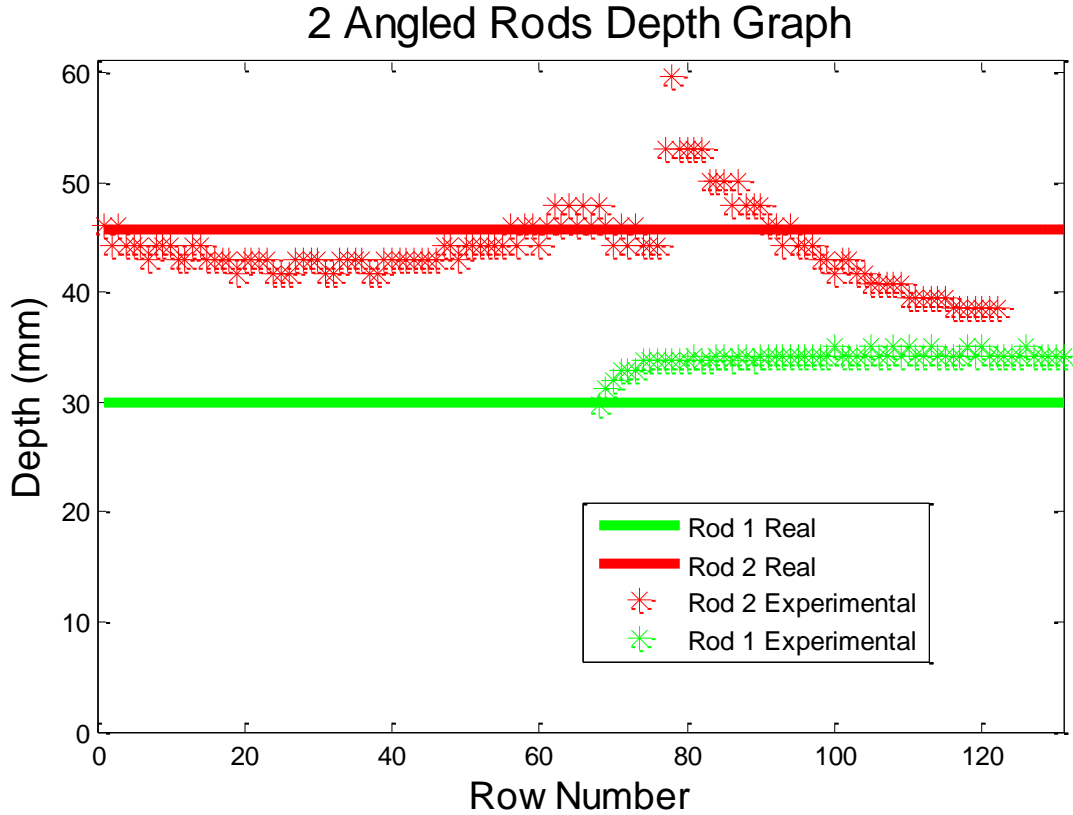
Figure 4.16 2nd derivative image of second two rod orientation used for Case IV (top). Depth results for both orientations of the second rod; parallel (middle) and angled (bottom).

Chapter V Conclusion & Discussion

4.1 Conclusion

The focus of this study was to assess how sensitive the calibration curves were to variations in the parameters used in the simulation software used to derive them, and also investigate the performance of the image processing and depth discrimination algorithms for different orientations of rod structures. After deriving calibration curves for variations in optical properties, off-axis detector distance, source position, and medium geometry, it was found that the curves were the most sensitive to the medium geometry selection. In contrast, parameters

such as off-axis detector distance and source position in relation to the detectors in the x-y plane had sufficient margins of error so as to not cause a drastic change in the calibration curve.

To test the effectiveness of the calibration curves in discriminating depth, both a solid phantom and liquid phantom were used. However, the limitations of rod orientation and the fact that white Delrin rods were detectable in the raw data images forced us to use solely the liquid phantom to assess the efficacy of depth discrimination. Through experimentation on different rod arrangements within the liquid phantom, it was concluded that the angle of the rod in the x-y plane has negligible effect on the depth calculation. It was also found that the calibration used to calculate the depths undercalculate the depth for shallower and middle regions, while deeper regions become more accurate.

4.2 Discussion

The 2D planar scan offers an advantage over diffuse optical tomography due to its applicability with spectroscopy and also the high spatial resolution that is possible in the x-y plane of the image space. The latter was the subject of this study as our overall motivation was to increase the spatial resolution of diffuse optical mammography images so that doctors and radiologists will be able to discern more structural and morphological information of the obstructions within the breast tissue being imaged. Specifically, this study tested and assessed a depth discrimination method that was developed to distinguish the depth coordinate of the inhomogeneities mapped into the 2D projection image that is the result of the planar scan. The method associates the off-axis shift between the spatial location of an inhomogeneity such as a rod to an effective depth. Therefore, much of this study was focused on testing the accuracy of the calculated depth for a given rod orientation within a liquid phantom.

However, before we could test the effectiveness of the depth discrimination method for different rod orientations in the medium, we had to assess the effect of certain parameters to the calibration curve with which we use to derive depth. The parameters that were tested were optical properties, medium geometry, off-axis detector separation distance, x-y spatial location of the source. It was found that the calibration curves experience negligible error for variations in optical properties that are typically found in breast tissue, and also for the off-axis detector separation distance. The former is especially crucial as this means that the optical properties of the liquid phantom do not have to be measured so long as the volumetric ratio used in [12] was used when mixing the 2% reduced fat milk and water. Additionally, breast tissue is not a homogeneous mixture like infinite geometry mediums which was the medium used to derive the calibration curve for the liquid phantom cases. Knowing that there is negligible error due to any realistic discrepancy in optical properties between breast tissue and liquid phantom gives us confidence that any inconsistency between calculated and actual depth is most probably due to another factor other than optical properties.

We also determined that the source position in the x-y plane does not cause any error in the calibration curve so long as it is on the axis of the detector pair for which the calibration curve was derived for. However, there was a noticeable increase in error as the source position is moved in the direction that is perpendicular to the detector pair in question. The margin of error in this axis was found to be ~3 mm. This was advantageous for our experiments as it provided a limit to the error in source placement that was achievable by adjusting the source by hand.

The parameter which lead to the most noticeable discrepancy between calibration curves was the medium geometry. It was found that the majority of the calibration curve for the slab

geometry was lower than that of the infinite medium geometry. Thus, this means that the medium geometry needs to be taken into account every time a scan is performed. Furthermore, this may be significant when moving from liquid phantom scans to clinical trials as human breasts exhibit a slab geometry when embedded between source-detector plates.

Ultimately, the depth discrimination algorithm relies greatly on the calibration curve used to associate the calculated shift with a specific depth value. In fact, even if the off-axis shift between the two detectors can be accurately measured for a particular inhomogeneity, if the calibration curve is not tailored to the specific geometry and source-detector configuration that is used for the experiment it could systematically affect all of the results. For instance, in Case II of the depth discrimination results (Section 4.3.2) there is a noticeable error for all the angles of approximately +8 mm. Because the depth values are consistent between each angle, there are two conclusions we can make. For one, the angle of the rod in the x-y plane does not seem to affect the off-axis shift experienced between the detectors. Secondly, the simulations run by the D&P software to derive the calibration curves, must not adequately replicate the medium, inhomogeneity, or source-detector configuration used in the experiments. The results from calibration curve experiments prove to us that variations in optical property range and even the source-detector configuration parameters such as the total medium thickness, D, source position, and off-axis detector distance, δD are unlikely causes for this error. Therefore, the most probable cause of this error is the classification of the inhomogeneity as point-like in the D&P software instead of a rod. Although the exact effect of the inconsistency between inhomogeneity geometry on off-axis shift is not known, the propagation characteristic of incident light on a point-like inhomogeneity and a rod inhomogeneity is clearly different. Specifically, photons incident on a point-like inhomogeneity is allowed to scatter in all directions in the x-y plane,

while photons incident on a rod have the possibility of being absorbed by other areas of the rod that are adjacent to the area that is exposed to NIR light.
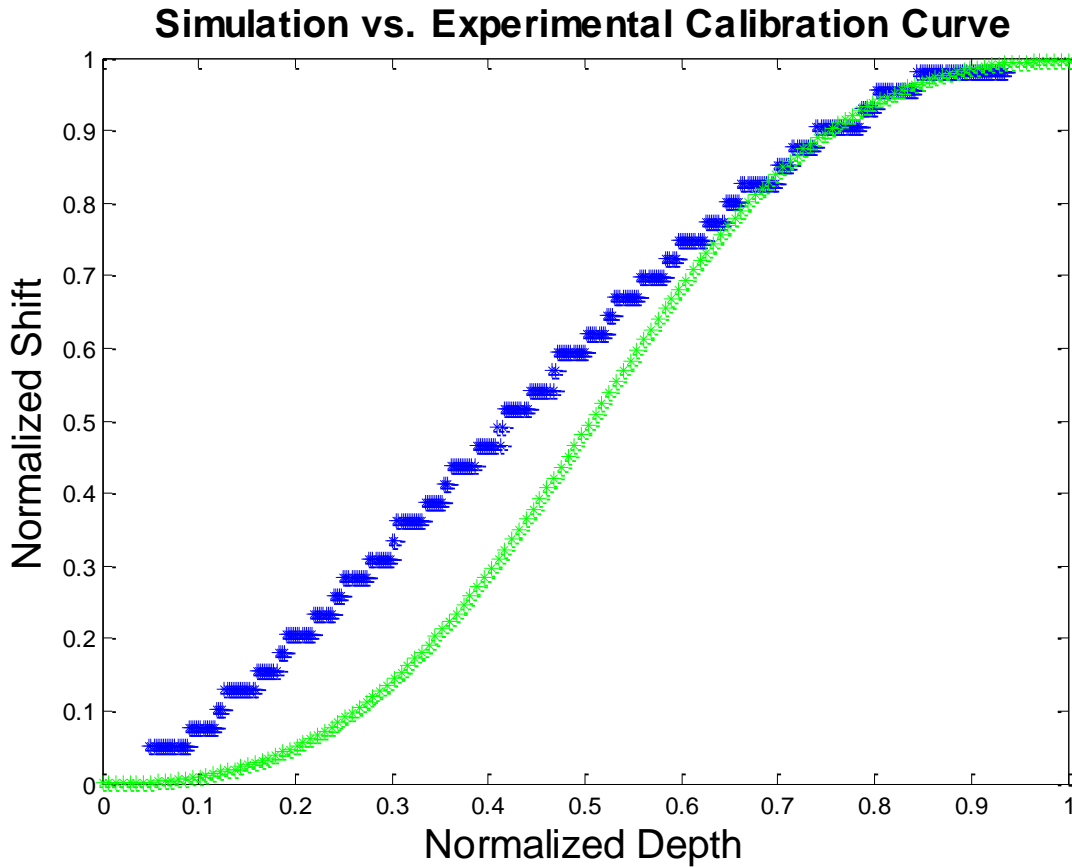

Figure 5.1 Comparison between experimental and simulation calibration curves. Green - curve from D&P software. Blue - curve derived through experimentation.

For this reason, one of our last experiments was to confirm the calibration curve used for this experiment by actually performing the line scans that the D&P software does to obtain the optical curves for each inhomogeneity depth. However, for our experiment we used a rod structure instead of a point-like inhomogeneity and the spatial sampling rate of the PMTs were .5 mm^{-1} instead of 75 mm^{-1} used in the D&P software. Therefore, as can be seen in Figure 5.1, the resolution of the off-axis shift is significantly less than the calibration curve derived through

simulations. However, there is a high observable error between the two curves, especially for normalized depths below .6. Interestingly, if the new experimental calibration curve is used to deduce the depths of the rods in the experiments, the calculated depths for the shallower and middle regions will be higher than that using the simulation calibration curve. This is consistent with our results from Case I where we experience the majority of the error in the shallower depths and as the inhomogeneity gets deeper the error decreases significantly. Figure 5.2 shows the depth results for Case I of the depth experiments using the experimental calibration curve.
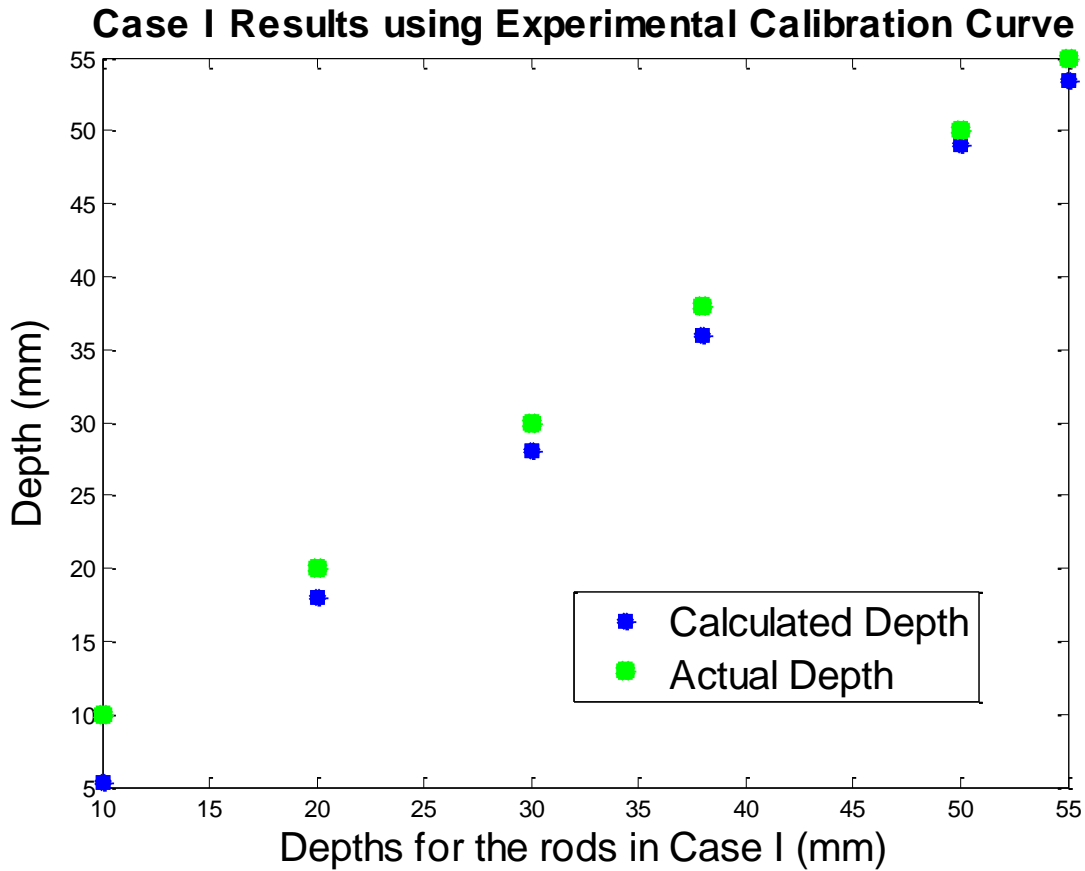

Figure 5.2 Depth results for Case I using experimental calibration curve.

4.3 Future Work

      There are several improvements, changes, and additions to the experimental protocol of this study that may improve the performance of the depth discrimination algorithm. For one, there needs to be a more thorough investigation as to why the simulated calibration curve is not consistent with the experimental calibration curve presented in the last section. The experimental calibration curve proves to us that the off-axis shifts have a unique positive correlation with depth. However, performing the scan to acquire the experimental curve for each experiment is not only not practical for a liquid phantom, it is not possible in a clinical setting. The best route would be to repeat all the simulations for the calibration curve using user-programmed Monte Carlo simulations where the user has more control over the shape of the inhomogeneity.
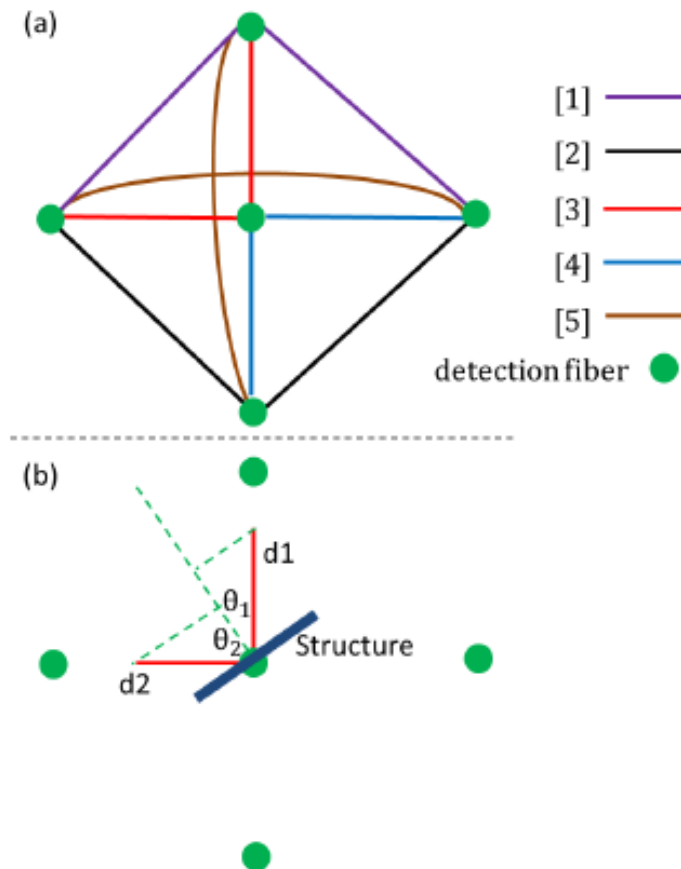
Figure 5.3 Method presented in [12] that uses an average of 5 detector pair depth calculations to measure depth.

Another possible area for improvement is the functionality of the four off-axis detectors used in the majority of the experiments. Especially for cases in which a rod structure is angled along the depth direction, it is important that we develop a method that could utilize the information from all four detectors to make a depth calculation. [12] has proposed a method in which four off-axis detectors and one on-axis detector is used to calculate the depth. The detectors are grouped into 5 pairs and the direction of the offset between the two images for a particular detector pair is perpendicular to each other. Using the Pythagorean Theorem, the depth for each detector pair, i, will be calculated using the following expression:

$$Depth_i = \sqrt{(d_1 cos\theta_1)^2 + (d_2 cos\theta_2)^2} \tag{5.1}$$

where d_1 and d_2 are the off-axis distances for the detector pair and θ_1 and θ_2 are the angles between the direction of the off-axis distance and the line perpendicular to the rod structure (Figure 5.3). The effective depth value is the average of all five depth values calculated using 5.1. The added advantage of using this method to discriminate depth is that it may possibly lead to more accurate depth calculations for rods that are angled in the depth direction, as all the detector pairs are taken into account for the calculation. However, to use this expression it is necessary for us to develop a method of find the angles θ_1 and θ_2. This can be accomplished by calculating the magnitude and direction of the gradient using a modified version of the second derivative algorithm, as the direction perpendicular to the rod structure is the direction of the highest gradient.

Although further experiments with simple orientations of rod structures should still continue, more complicated structural arrangements involving more than two rods can be implemented. This can either be done through the use of the liquid phantom like the experiments of this study, or through silicon molds which provide the flexibility of arranging the rods in various orientations while still achieving the slab geometry that is a more valid description of the geometry used for 2D planar scans of breast tissue. Also, the added structures could be made out of a different material other than Delrin that is more flexible, allowing for curvature of the obstructions. The implementation of a network of structures is important especially because it can validate the efficacy of the maximum dot product method of finding the off-axis shift described in Section 1.2.5. The rod orientations for the experiments of this study proved to be too simple to test the efficacy of the maximum dot product method as there was at most two rods in the phantom at a time. This method is meant for more complicated arrangements where it is not practical to visually locate the off-axis peaks of the obstructions that are to be resolved in the depth direction.

References

1. "U.S. Breast Cancer Statistics." *BreastCancer.org*. N.p., n.d. Web. 11 Mar. 2012.

   <http://www.breastcancer.org/symptoms/understand_bc/statistics.jsp>.

2. "CDC - Breast Cancer Statistics." *Center for Disease Control and Prevention*. N.p., n.d. Web.

   <http://www.cdc.gov/cancer/breast/statistics/index.htm>.

3. "WHO Breast cancer: prevention and control." *World Health Organization*. N.p., n.d. Web.

   <http://www.who.int/cancer/detection/breastcancer/en/index1.html>.

4. Brewer, Noel T., Talya Salz, and Sarah E. Lillie. "Systematic Review: The Long-Term

   Effects of False-Positive Mammograms." *Annals of Internal Medicine* 146 (2007): 502-

   10. Print.

5. Cyrlak, D. "Induced Costs of Low-Cost Screening Mammography." *Radiology*: 661-63. Print.

6. Carpenter, C. M., et al. "MRI-guided Near-infrared Spectroscopy of Breast Tumors."

   Medicamundi 53.1 (2009): 28-34. Print.

7. Time-Resolved Optical Tomography Instrumentation for Fast 3D Functional Imaging

   David K. Jennions. "Time-Resolved Optical Tomography Instrumentation for Fast 3D

   Functional Imaging." Diss. U of College London. *Dissertations and Theses.* January

   2008

8. Hillman, Elizabeth M., et al. "Time Resolved Optical Tomography of the Human Forearm."

   Physics in Medicine and Biology 46 (2001): 1117-30. Print.

9. Enfield, Louise C., et al. "Thee-dimensional Time-resolved Optical Mammography of the

   Uncompressed Breast." *Applied Optics* 46.17 (2007): 3629-38. Print.

10. Dirk Grosenick, K. Thomas Moesta, Heidrun Wabnitz, Jörg Mucke, Christian Stroszczynski, Rainer Macdonald, Peter M. Schlag, and Herbert Rinneberg, "Time-Domain Optical Mammography: Initial Clinical Results on Detection and Characterization of Breast Tumors," Appl. Opt. **42**, 3170-   3186 (2003)

11. Grosenick, Dirk, et al. "Concentration and Oxygen Saturation of Haemoglobin of 50 Breast Tumours Determined by Time-Domain Optical Mammography." *Physics in Medicine and Biology* 49 (2004): 1165-81. Print.

12. Yang Yu. "Diffuse Optical Imaging and Spectroscopy of the Human Breast for Quantitative Oximetry with Depth Resolution." Diss. Tufts University. *Dissertations and Theses.* April 2011

13. D. Grosenick, H. Wabnitz, K. T. Moesta, J. Mucke, P. M. Schlag, and H. Rinneberg, "Time-domain scanning optical mammography: II. Optical properties and tissue parameters of 87 carcinomas," Phys. Med. Biol. 50, 2451-2468 (2005).

14. Schmitz, Christoph H., et al. "Design and Implementation of Dynamic Near-Infrared Optical Tomographic Imaging Instrumentation for Simultaneous Dual-breast Measurements." *Applied Optics* 44.11 (2005): 2140-53. Print.

15. Choe, Regina, Soren D. Konecky, and Alper Corlu. "Differentiation of Benign and Malignant Breast Tmors by in-vivo Three-dimensional Parallel-plate Diffuse Optical Tomography." *Journal of Biomedical Optics* 14.2 (2009): n. pag. Print.

16. T.J. Brukiliacchio. "Time-Domain Diffuse Optical Tomography for Breast Imaging". *Dissertations and Thesis.* 2003